The Astrophysical Journal, 971:119 (22pp), 2024 August 10 https://doi.org/10.3847/1538-4357/ad5294
© 2024. The Author(s). Published by the American Astronomical Society.
OPEN ACCESS

Measuring the Conditional Luminosity and Stellar Mass Functions of Galaxies by Combining the Dark Energy Spectroscopic Instrument Legacy Imaging Surveys Data Release 9, Survey Validation 3, and Year 1 Data

Yirong Wang (王艺蓉)[1], Xiaohu Yang (杨小虎)[1,2], Yizhou Gu (顾一舟)[1], Xiaoju Xu (徐笑菊)[1], Haojie Xu (许浩杰)[1,3], Yuyu Wang (王钰钰)[1], Antonios Katsianis[1,4], Jiaxin Han (韩家信)[1], Min He (何敏)[1], Yunliang Zheng (郑云亮)[1], Qingyang Li (李清洋)[1], Yaru Wang (王雅茹)[1], Wensheng Hong (洪文生)[1], Jiaqi Wang (王佳琪)[1], Zhenlin Tan (谭镇林)[1], Hu Zou (邹虎)[5], Johannes Ulf Lange[6,7,8,9], ChangHoon Hahn[10,11], Peter Behroozi[12], Jessica Nicole Aguilar[13], Steven Ahlen[14], David Brooks[15], Todd Claybaugh[13], Shaun Cole[16], Axel de la Macorra[17], Biprateep Dey[18], Peter Doel[15], Jaime E. Forero-Romero[19,20], Klaus Honscheid[21,22], Robert Kehoe[23], Theodore Kisner[13], Andrew Lambert[13], Marc Manera[24,25], Aaron Meisner[26], Ramon Miquel[24,27], John Moustakas[28], Jundan Nie[5], Claire Poppett[13,29], Mehdi Rezaie[30], Graziano Rossi[31], Eusebio Sanchez[32], Michael Schubnell[8], Gregory Tarlé[33], Benjamin Alan Weaver[26], and Zhimin Zhou[5]

[1] Department of Astronomy, School of Physics and Astronomy, and Shanghai Key Laboratory for Particle Physics and Cosmology, Shanghai Jiao Tong University, Shanghai 200240, People's Republic of China; wyirong@sjtu.edu.cn, xyang@sjtu.edu.cn
[2] Tsung-Dao Lee Institute, and Key Laboratory for Particle Physics, Astrophysics and Cosmology, Ministry of Education, Shanghai Jiao Tong University, Shanghai 200240, People's Republic of China
[3] Shanghai Astronomical Observatory, Chinese Academy of Sciences, Nandan Road 80, Shanghai 200240, People's Republic of China
[4] School of Physics and Astronomy, Sun Yat-sen University, Zhuhai Campus, 2 Daxue Road, Xiangzhou District, Zhuhai, People's Republic of China
[5] National Astronomical Observatories, Chinese Academy of Sciences, A20 Datun Road, Chaoyang District, Beijing, 100012, People's Republic of China
[6] Kavli Institute for Particle Astrophysics and Cosmology and Department of Physics, Stanford University, CA 94305, USA
[7] Department of Astronomy and Astrophysics, University of California, Santa Cruz, CA 95064, USA
[8] Department of Physics, University of Michigan, Ann Arbor, MI 48109, USA
[9] Leinweber Center for Theoretical Physics, University of Michigan, Ann Arbor, MI 48109, USA
[10] Department of Astrophysical Sciences, Princeton University, Peyton Hall, Princeton, NJ 08544, USA
[11] Lawrence Berkeley National Laboratory, One Cyclotron Road, Berkeley, CA 94720, USA
[12] Department of Astronomy and Steward Observatory, University of Arizona, Tucson, AZ 85721, USA
[13] Lawrence Berkeley National Laboratory, 1 Cyclotron Road, Berkeley, CA 94720, USA
[14] Physics Department, Boston University, 590 Commonwealth Avenue, Boston, MA 02215, USA
[15] Department of Physics & Astronomy, University College London, Gower Street, London, WC1E 6BT, UK
[16] Institute for Computational Cosmology, Department of Physics, Durham University, South Road, Durham DH1 3LE, UK
[17] Instituto de Física, Universidad Nacional Autónoma de México, Cd. de México C.P. 04510, Mexico
[18] Department of Physics & Astronomy and Pittsburgh Particle Physics, Astrophysics, and Cosmology Center (PITT PACC), University of Pittsburgh, 3941 O'Hara Street, Pittsburgh, PA 15260, USA
[19] Departamento de Física, Universidad de los Andes, Cra. 1 No. 18A-10, Edificio Ip, CP 111711, Bogotá, Colombia
[20] Observatorio Astronómico, Universidad de los Andes, Cra. 1 No. 18A-10, Edificio H, CP 111711 Bogotá, Colombia
[21] Department of Physics, The Ohio State University, 191 West Woodruff Avenue, Columbus, OH 43210, USA
[22] Center for Cosmology and AstroParticle Physics, The Ohio State University, 191 West Woodruff Avenue, Columbus, OH 43210, USA
[23] Department of Physics, Southern Methodist University, 3215 Daniel Avenue, Dallas, TX 75275, USA
[24] Institut de Física d'Altes Energies (IFAE), The Barcelona Institute of Science and Technology, Campus UAB, 08193 Bellaterra Barcelona, Spain
[25] Departament de Física, Serra Húnter, Universitat Autònoma de Barcelona, 08193 Bellaterra (Barcelona), Spain
[26] NSF's NOIRLab, 950 North Cherry Avenue, Tucson, AZ 85719, USA
[27] Institució Catalana de Recerca i Estudis Avançats, Passeig de Lluís Companys, 23, 08010 Barcelona, Spain
[28] Department of Physics and Astronomy, Siena College, 515 Loudon Road, Loudonville, NY 12211, USA
[29] Space Sciences Laboratory, University of California, Berkeley, 7 Gauss Way, Berkeley, CA 94720, USA
[30] Department of Physics, Kansas State University, 116 Cardwell Hall, Manhattan, KS 66506, USA
[31] Department of Physics and Astronomy, Sejong University, Seoul, 143-747, Republic of Korea
[32] CIEMAT, Avenida Complutense 40, E-28040 Madrid, Spain
[33] University of Michigan, Ann Arbor, MI 48109, USA

Received 2023 December 3; revised 2024 May 6; accepted 2024 May 29; published 2024 August 9

Abstract

In this investigation, we leverage the combination of the Dark Energy Spectroscopic Instrument (DESI) Legacy Imaging Surveys Data Release 9, Survey Validation 3, and Year 1 data sets to estimate the conditional luminosity functions and conditional stellar mass functions (CLFs and CSMFs) of galaxies across various halo mass bins and redshift ranges. To support our analysis, we utilize a realistic DESI mock galaxy redshift survey (MGRS) generated from a high-resolution Jiutian simulation. An extended halo-based group finder is applied to both MGRS catalogs and DESI observation. By comparing the *r*- and *z*-band luminosity functions (LFs) and stellar mass functions (SMFs) derived using both photometric and spectroscopic data, we quantified the impact of photometric redshift (photo-*z*) errors on the galaxy LFs and SMFs, especially in the low-redshift

Original content from this work may be used under the terms of the Creative Commons Attribution 4.0 licence. Any further distribution of this work must maintain attribution to the author(s) and the title of the work, journal citation and DOI.

bin at the low-luminosity/mass end. By conducting prior evaluations of the group finder using MGRS, we successfully obtain a set of CLF and CSMF measurements from observational data. We find that at low redshift, the faint-end slopes of CLFs and CSMFs below $\sim 10^9\, h^{-2}\, L_\odot$ (or $h^{-2}\, M_\odot$) evince a compelling concordance with the subhalo mass functions. After correcting the cosmic variance effect of our local Universe following Chen et al., the faint-end slopes of the LFs/SMFs turn out to also be in good agreement with the slope of the halo mass function.

Unified Astronomy Thesaurus concepts: Dark matter (353); Large-scale structure of the universe (902); Galaxies (573); Galaxy groups (597); Galaxy dark matter halos (1880)

1. Introduction

Over the past few decades, large galaxy surveys, such as the Two-degree Field Galaxy Redshift Survey (2dFGRS; Colless 1999) and Sloan Digital Sky Survey (SDSS; York et al. 2000), have played a significant role in advancing our understanding of galaxy formation and evolution. These surveys allow for various galaxy observable measurements, including the luminosity function (LF), stellar mass function (SMF), and two-point correlation function (Norberg et al. 2002; Blanton et al. 2003; Zehavi et al. 2005, 2011; Wang et al. 2007, 2021; Li & White 2009; Zhao et al. 2020; Moustakas et al. 2013). Despite the absence of direct physical explanations of galaxy formation and evolution, the statistical measurements provide essential constraints on multiple physical processes, including gravitational instability, gas cooling, star formation, merging, tidal stripping, heating, and feedback mechanisms. However, modeling the galaxy observables through physical processes remains a challenge, given the incomplete understanding of these processes (Naab & Ostriker 2017; Smercina et al. 2018; Katsianis et al. 2021; Sales et al. 2022).

Under the hypothesis that galaxies form within dark matter halos, empirical halo models provide a straightforward way to model galaxy observables and infer the relationship between galaxies and their host halos (Wechsler & Tinker 2018; Katsianis et al. 2023). For instance, the halo occupation distribution (HOD; Jing et al. 1998; Peacock & Smith 2000; Tinker et al. 2005; Zheng et al. 2005, 2009; Brown et al. 2008; Zu & Mandelbaum 2015, 2016, 2018; Wang et al. 2019; Yuan et al. 2018, 2022; Alam et al. 2020) infers the number of galaxies of a specific type in halos of different masses, and the conditional luminosity function (CLF; van den Bosch et al. 2003, 2007; Yang et al. 2003, 2008, 2012; Cacciato et al. 2009) constrains the galaxy LFs in halos of different masses. Additionally, the subhalo abundance matching (SHAM; Vale & Ostriker 2004; Conroy et al. 2006; Behroozi et al. 2010; Neistein et al. 2011; Guo et al. 2016) links the number density of galaxies above a luminosity (or stellar mass) threshold to the number density of subhalos above a mass (or circular velocity) threshold. These empirical models have significantly enhanced our understanding of the galaxy formation and evolution processes.

In addition to studies of the galaxy–halo connection through model fittings based on statistical measurements, an alternative method is introduced to identify individual dark matter halos observationally and measure the galaxy content within them. To this end, the halo-based group-finding algorithm (Yang et al. 2005b) has particular advantages in grouping galaxies within the same dark matter halos, and it has been extensively tested and applied to galaxy samples with spectroscopic redshifts (Yang et al. 2005b, 2007). The original version of the group finder estimates halo mass using the total luminosity inside each group. However, the accuracy may decrease for groups with few members, especially for a very shallow survey like 2MRS (Huchra et al. 2012). Other halo mass estimations are proposed to address this issue, for example, using the luminosity gap between the central and satellite or the luminosity–halo mass relation from hydrodynamic simulation (Lu et al. 2015; Lim et al. 2017). Other observables, such as the total luminosity of satellites in a halo, can also be used to estimate halo mass (Tinker 2021; Tinker et al. 2021). Additionally, halo mass estimation can also be improved by considering the bimodality of star formation or color (Old et al. 2014, 2015; Rodríguez-Puebla et al. 2015; Tinker 2021). These methodologies have demonstrated success in low-redshift surveys with high spectroscopic redshift completeness.

Apart from proposing different halo mass estimation methods, an alternative way to improve the halo mass estimation accuracy is to make use of faint galaxies in photometric redshift surveys. Within this framework, Yang et al. (2021) extended the halo-based group finder so that it can deal with galaxies with photometric and spectroscopic redshifts simultaneously, which significantly broadened its application scope. Based on the increasing applicability of the group finder, the CLFs and conditional stellar mass functions (CSMFs) have been successfully measured from the 2dFGRS, SDSS, Hyper Suprime-Cam, and DECam Legacy Survey (DECaLS) observations. However, these measurements predominantly pertain to low redshifts and relatively luminous galaxies (e.g., Yang et al. 2005a, 2008, 2009; Lan et al. 2016; To et al. 2020; Tinker et al. 2021; Wang et al. 2021; Golden-Marx et al. 2023; Meng et al. 2023).

In this study, we explore the LFs, SMFs, CLFs, and CSMFs (central and satellite) of galaxies across different halo mass bins and redshift ranges through galaxy and group catalogs constructed by Yang et al. (2021) from the Dark Energy Spectroscopic Instrument Legacy Imaging Surveys Data Release 9 (DESI LS DR9) sample in the redshift range of $z = [0, 1]$, which has a selection of apparent magnitudes down to $m_z = 21$. We seek to evaluate the impact of photometric redshift and spectroscopic completeness on the LFs and SMFs, with a particular focus on the faint end, by making full use of the first year of spectroscopic observation data. Furthermore, we utilize a DESI mock galaxy redshift survey (MGRS; Gu et al. 2024) based on Jiutian, a high-precision N-body simulation (see more details in Section 4.1), to perform the same statistical measurements using the same group finder employed in DESI observations, which facilitates the evaluation of systematic biases and allows for a more accurate investigation of the history of galaxy formation and evolution in future studies. Our galaxy samples are subject to observational effects, particularly in terms of the spectroscopic sampling. With the benefit of the extension version of the group finder, we expect more reliable CLFs and CSMFs from DESI observations guided by simulated mock data.

In Section 2, we detail the photometric and spectroscopic data, including the construction of group catalogs and the sample selection for estimations of LFs, SMFs, CLFs, and CSMFs implemented in this paper. In Section 3, we investigate the impact of photo-z errors on the measurements of LFs and SMFs. In Section 4, we use an MGRS to provide reliability verification of CLF measurements based on groups detected by the group finder. In Section 5, we present the CLFs and CSMFs based on the observational data. Finally, we discuss and summarize our results in Sections 6 and 7.

Throughout this paper, we use ΛCDM cosmology with parameters that are consistent with the Planck 2018 results (Planck Collaboration et al. 2020): $\Omega_m = 0.315$, $\Omega_\Lambda = 0.685$, $h = H_0/(100\,\mathrm{km\,s^{-1}\,Mpc^{-1}}) = 0.674$, and $\sigma_8 = 0.811$. Unless otherwise specified, luminosity (stellar mass) and halo masses are presented in units of $h^{-2}\ L_\odot$ ($h^{-2}\ M_\odot$) and $h^{-1}\ M_\odot$, respectively. The luminosity (stellar mass) functions are presented in units of $h^3\,\mathrm{Mpc}^{-3}\,d\log L$ ($h^3\,\mathrm{Mpc}^{-3}\,d\log M$), where log is the base 10 logarithm. The units of the conditional luminosity (stellar mass) function are $d\log L/\mathrm{group}$ and $d\log M/\mathrm{group}$.

2. Observational Data

In this section, we describe the construction of galaxy samples from the DESI observational data utilized in this study. The general overview and instrument of DESI can be found in a series of papers (DESI Collaboration et al. 2016a, 2016b, 2022; Levi et al. 2013; Silber et al. 2023; Miller et al. 2023). Overall, the galaxy sample is constructed by integrating a seed galaxy catalog, which is primarily based on the DESI LS, with the data gathered from previous spectroscopic surveys and DESI up to the first year of observation. Subsequently, group memberships are assigned using our extended adaptive halo-based group finder (e.g., Yang et al. 2005b, 2007, 2021).

2.1. DESI LS DR9

LS DR9 is the basis of the seed catalog, which includes three optical bands (grz) from the Beijing–Arizona Sky Survey (Zou et al. 2017), the Mayall z-band Legacy Survey, and DECaLS (Dey et al. 2019). The DR9 also includes deeper optical data from the Dark Energy Survey (The Dark Energy Survey Collaboration 2005). The optical bands of LS DR9 provide a 5σ detection of 24/23.4/22.5 AB magnitude with a half-light radius of $0\farcs45$. The target selections and survey validation of the DESI observational data are described in detail in DESI Collaboration et al. (2023, 2024), Lan et al. (2024), Alexander et al. (2023), Cooper et al. (2023), Hahn et al. (2023), Zhou et al. (2020, 2023), Raichoor et al. (2020, 2023), Chaussidon et al. (2023), Allende Prieto et al. (2020), Ruiz-Macias et al. (2020), Yèche et al. (2020), and Myers et al. (2023). We use the photometric redshift (photo-z) from the Photometric Redshifts for the Legacy Surveys (PRLS) catalog (Zhou et al. 2021), which estimates photo-z by combining optical and mid-infrared photometry (W1 3.4 μm and W2 4.6 μm) from the Wide-field Infrared Survey Explorer (WISE). Zhou et al. (2021) demonstrate that the reliability of photo-z estimation decreases beyond a z-band apparent magnitude of $m_z \simeq 21$. Therefore, the apparent magnitude of the z band of our primary galaxy sample is limited to $m_z \leqslant 21$. Although the overall selection of galaxies for this study closely follows that of Yang et al. (2021), a few modifications have been implemented to accommodate the transition from LS DR8 to LS DR9. Details about our sample selection are outlined below.

To mitigate the potential contamination, it is imperative to exclude stars and active galactic nuclei (AGNs) from galaxy samples. Benefitting from the morphological classification that identifies six distinct morphological types in DR9,[34] we start by eliminating objects of the PSF and DUP[35] types from the galaxy sample. The remaining extended sources with morphological classifications of REX, EXP, DEV, and COMP[36] make up our galaxy sample (similar to Yang et al. 2021).

To ensure the photometric quality of our objects, constraints are imposed following similar procedures as those described in Zou et al. (2019, 2020, 2021), Ruiz-Macias et al. (2020), Raichoor et al. (2020), Yèche et al. (2020), and Moustakas et al. (2023). We require that each object has at least one exposure in each optical band. Objects located near the Galactic plane ($b < 25°$, where b is the Galactic latitude) are eliminated to avoid regions of high stellar density. Additionally, the following bit numbers in the MASKBITS columns are used: 1 (close to Tycho-2 and Gaia bright stars); 5, 6, and 7 (close to objects that have the ALLMASK_[G, R, Z] bits set); 8 (close to WISE W1 bright stars); 9 (close to WISE W2 bright stars); 11 (close to fainter Gaia stars); and 12 and 13 (close to a local large galaxy and globular cluster, respectively). We use these selection conditions to remove the objects that are contaminated or blended. In addition to the MASKBITS, other quality flags are employed to remove the flux contaminations from nearby sources (FRACFLUX) or masked pixels (FRACMASKED):

$$\begin{aligned} \mathrm{FRACMASKED}_X &< 0.4, \\ \mathrm{FRACIN}_X &> 0.3, \\ \mathrm{FRACFLAX}_X &< 0.5, \end{aligned}$$

where $X = g$, r, and z. The purpose of FRACIN is to select the objects for which a large fraction of the model flux is in the contiguous pixels where the model was fitted. Note that all the magnitudes used in this paper are in the AB system and have been corrected for Galactic extinction by using the Galactic transmission values provided in DR9.

Following these criteria, we obtain a seed catalog of 138,315,649 galaxies. Most of these galaxies only contain photometric redshifts, which are the median values of the photo-z, z_phot_median, from the PRLS catalog. Approximately 3.7 million galaxies include spectroscopic redshifts collected from previous redshift surveys by Zhou et al. (2021) and Lim et al. (2017). The redshifts and properties of the galaxies are updated using the DESI spectroscopic data in Section 2.2.

2.2. DESI Spectroscopic Data and Group Finder

We make use of the most recent spectroscopic observation data (up to the first year of observation) from the

[34] This classification is facilitated by a software package called THE TRACTOR, as referenced in Lang et al. (2016). THE TRACTOR is also used for source detection and optical photometry. See more details at https://www.legacysurvey.org/dr9/description/##morphological-classification.

[35] PSF stand for point-spread function, and DUP indicates Gaia sources that are coincident with an extended source.

[36] REX denotes round exponential galaxies with a variable radius. EXP indicates exponential profiles (spiral galaxies). DEV represents de Vaucouleurs profiles (elliptical galaxies), and COMP indicates composite profiles combining de Vaucouleurs and exponential components.

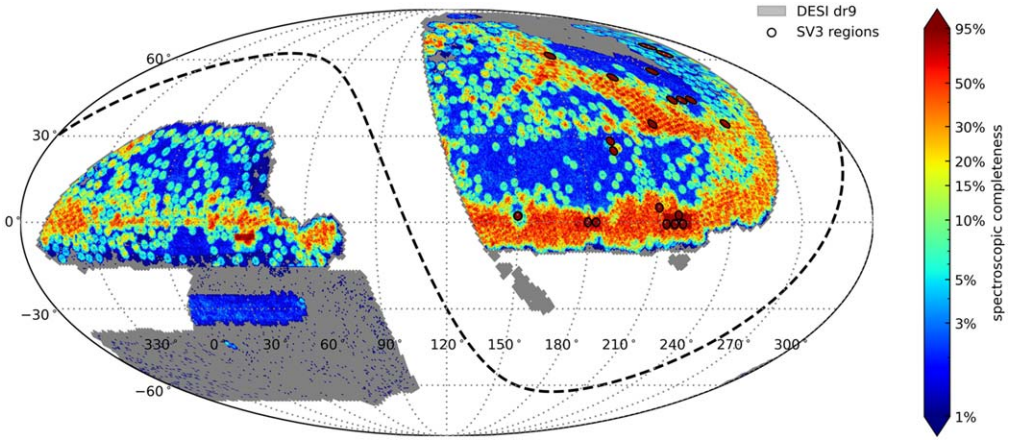

Figure 1. The sky coverage of the DESI spectroscopic data used in this study, where the spectroscopic completeness is calculated with respect to the total number of galaxies with $m_r \leqslant 19.5$. The gray footprints are the DESI LS DR9, which retains Galactic latitude $|b| > 25°$. SV3 regions are marked by black circles, which exhibit extremely high completeness. Some regions with low completeness are discretely distributed due to the collection of DESI Y1, SDSS, and other spectroscopic data. The black dashed line represents the Galactic plane.

`fastspecfit` value-added catalogs (version 1.0[37,38,39]), which contain three spectroscopic products, Fuji, Guadalupe, and Iron (e.g., Guy et al. 2023; Brodzeller et al. 2023; Moustakas 2023; Schlafly et al. 2023). Iron is the most comprehensive collection of spectral data available, containing 7.8 million galaxy spectra. We combine the fitting results of Fuji, Guadalupe, and Iron. For a galaxy with a unique target ID but multiple observations, we use the recommended "best" redshift with high quality in the combined catalogs across surveys and programs. The DESI LS guides the fiber assignment of the DESI spectroscopic survey. Therefore, our seed catalog, which primarily utilizes photometric redshift, can be updated with the measurements derived from DESI spectra. The updated seed catalog is used in the following analyses.

The extended group finder has been implemented to identify the membership of groups and estimate the group mass using both photometric and spectroscopic data. The group finder starts by considering each galaxy as a group candidate. The cumulative group LFs can then be measured, and halo mass is assigned to each group using an abundance matching method. Subsequently, halo radius and line-of-sight velocity dispersion are estimated based on this halo mass. Beginning with the most massive group, the member galaxies are identified in the region where the galaxy number density contrast is higher than a specific threshold. With the updated membership of the groups, both the group center and the total luminosity of the group can be updated, and the algorithm goes back to the step of measuring the group LF and assigning halo mass. The iteration continues until the mass-to-light ratios have converged.

We have noticed that 7.8% of the galaxies lack measurements in one or more of the five bands of $g/r/z/\mathrm{W1}/\mathrm{W2}$, despite having assigned photo-z values. Taking into account the much larger photo-z uncertainty of these galaxies than the typical values at $\sigma_{\mathrm{photo}} \sim (0.01 + 0.015z)(1+z)$, we have excluded them from the group-finding process and used a weight to correct this factor in the LF/SMF and CLF/CSMF measurements (see Section 3.1 for more details).

By applying the extended halo-based group finder to the updated seed catalog, a group catalog is created that covers a wide range of redshifts and halo masses. According to Yang et al. (2021), the extended halo-based group finder is highly successful in identifying more than 60% of the members in almost 90% of the halos with masses greater than $10^{12.5}\,h^{-1}\,M_{\odot}$ for galaxies with magnitudes $m_z \leqslant 21$ and photometric redshifts in the range $0 < z \leqslant 1.0$ in the DESI LS.[40] The group catalog provides useful information about the host halo properties of the galaxies, such as the halo mass and local environments and the central/satellite classification. Since most galaxies only have photometric redshifts, the entire sample is classified as LS DR9.

2.3. Sample Selection

In this paper, we consider three regions in the sky coverage with different levels of spectroscopic completeness.

1. The whole region of the updated seed galaxy catalog with a magnitude limit $m_z \leqslant 21$, constructed from LS DR9 and the DESI spectroscopic survey, which is primarily used to find the groups.
2. The Year 1 (Y1) region with a wide sky coverage of 12,276 deg^2 and an approximate ∼45% spectral completeness after the Bright Galaxy Survey (BGS) selection ($m_r \leqslant 19.5$ and $m_z \leqslant 19$), which is used to measure the CLFs and CSMFs.
3. The Survey Validation 3 (SV3) region with the highest spectral completeness (over 95%) after the bright magnitude cuts above, which is used as a benchmark to investigate the effect of photo-z on the LF and SMF measurements.

The SV3 region and the Y1 region are defined by a set of rosettes and tiles using caps at a given radius, respectively, while the overall footprint of the seed catalog is mapped using the healpix tool (Górski et al. 2005). This tool divides the spherical surface into subdivisions, each of which covers the same surface area. We set the parameter nside = 256, which corresponds to $5.246 \times 10^{-2}\,\mathrm{deg}^2$ per subdivision.

[37] https://fastspecfit.readthedocs.io/en/latest/fuji.html
[38] https://fastspecfit.readthedocs.io/en/latest/guadalupe.html
[39] https://fastspecfit.readthedocs.io/en/latest/iron.html

[40] Better performance can be achieved in a spectroscopic redshift sample (see Yang et al. 2007).

Table 1
Sample Definition and the Related Selection Criteria

Sample ID	Sky Coverage (deg^2)	Magnitude Cut (mag)	Redshift Cut	Total	Central	Satellite	Spec-z Percent
SV3-r19.5	133	$m_r \leqslant 19.5$	$z \leqslant 0.6$	93,943	73,785	20,158 (21.5%)	99.2%
SV3-z19.0	133	$m_z \leqslant 19.0$	$z \leqslant 0.6$	120,392	96,016	24,376 (20.2%)	95.2%
Y1-r19.5	12,276	$m_r \leqslant 19.5$	$z \leqslant 0.6$	8,464,733	6,484,281	1,980,452 (23.4%)	46.4%
Y1-z19.0	12,276	$m_z \leqslant 19.0$	$z \leqslant 0.6$	10,912,062	8,424,354	2,487,708 (22.8%)	44.3%

Subdivisions with at least one galaxy are treated as part of the footprint. Figure 1 shows the sky coverage of the spectroscopic data used in this study. The SV3 region is marked by black circles, while the Y1 region is indicated by the color gradient area from cyan to red. The color coding represents the spectroscopic completeness calculated with respect to the total galaxies of $m_r \leqslant 19.5$. The remaining regions, characterized by gray and blue, primarily lack spectroscopic data and mainly contribute to the group finder.

To ensure a higher rate of spectroscopic redshift completeness and a reasonable sampling, we restrict our analysis to the galaxy sample with $m_r \leqslant 19.5$ and $z \leqslant 0.6$, which is in line with the selection criteria of the DESI BGS. It has been verified that galaxies in our sample with $m_r \leqslant 19.5$ are almost identical to the targets of the BGS sample conducted by Hahn et al. (2023, 2024). Taking into account the magnitude difference between the r and z bands, this roughly corresponds to $m_z \leqslant 19.0$. Combining the footprint and apparent magnitude cut, we define four subsamples for our analysis and list the details in Table 1. In the first two, Y1-r19.5 and Y1-z19.0, nearly 45% of the galaxies have spectroscopic redshifts. For simplicity, we use Y1-BGS to refer to Y1-r19.5 or Y1-z19.0 depending on the band we are using.

Within the Y1 region, the DESI 1% Survey (also known as SV3, which includes three spectroscopic productions but covers a smaller area) has a significantly higher spectroscopic completeness, which is marked by black circles in Figure 1, and the spectroscopic completeness of the remaining area is relatively lower. The SV3 strategy was mainly focused on guiding and validating the survey design. To achieve a high level of completeness, additional passes were performed for each of the 20 rosettes within SV3. These passes covered an area of more than 7 deg^2, extending up to 1.°45 from the center of each discrete region. Among these 20 rosettes, one rosette with celestial coordinates (194.75, 28.20) is centered in the Coma cluster. As we will demonstrate in Figure A2 in Appendix A, the inclusion of this rosette will significantly enhance the LFs (or SMFs) at $L \sim 10^8\, h^{-2}\, L_{\odot}$, resulting in considerable cosmic variances. Consequently, we opted to exclude this rosette from our LF and SMF measurements. By applying the BGS selections mentioned above, the spectroscopic redshift completeness is overall larger than 95% with 133 deg^2 sky coverage. Here again, for simplicity, we use SV3-BGS to represent the third and fourth subsamples SV3-z19.0 or SV3-r19.5, depending on the band we are using. Despite the relatively limited sky coverage and the disconnection of SV3-BGS, the high-redshift completeness allows for the verification of the impact of photo-z errors on LF and SMF measurements.

The group catalogs of the SV3 and Y1 subsamples are extracted from those of LS DR9. The detailed selection criteria and the total number of galaxies, as well as the number of central and satellite galaxies in our four subsamples, are listed in Table 1. This enables us to distinguish the contribution of centrals and satellites to the CLF, affording valuable insights into the distribution of galaxies within groups.

2.4. Galaxy Luminosity and Stellar Mass

Following Yang et al. (2021), for each galaxy passed to the group finder, we use the following function to convert apparent magnitude to absolute magnitude according to its redshift:

$$M^j{}_X - 5\log h = m_X - \mathrm{DM}(z_{\rm obs}) - K^j_X(z_{\rm obs}), \quad (1)$$

where X stands for the particular band (r or z) we adopted. K^j_X represents each galaxy's k-correction to the X band shifted by the band-shift redshift, j, where $j = 0.1$, 0.3, or 0.5 are obtained from the "Kcorrect" model (e.g., v4_3) described in Blanton & Roweis (2007). $\mathrm{DM}(z_{\rm obs})$ is the distance module corresponding to the redshift $z_{\rm obs}$, defined as

$$\mathrm{DM}(z_{\rm obs}) = 5\log D_L(z_{\rm obs}) + 25, \quad (2)$$

with $D_L(z_{\rm obs})$ being the luminosity distance in units of h^{-1} Mpc. The luminosity of each galaxy is then calculated using the following formula:

$$\log_{10} L^j_X = 0.4*(M^j{}_{\odot} - M^j{}_X). \quad (3)$$

For a better consideration of the absolute magnitude of the Sun after k-correction, $M^j_{\odot}$, we use the fitting results of the k-correction in narrow redshift bins from $z = 0$ to maximum redshift. These k-correction values at typical redshifts are listed below and are consistent with $M^{j=0}_{\odot}$ being 4.61 and 4.5 in the r and z bands, respectively (Willmer 2018):

$$K^{[0.1,0.3,0.5]}_{\odot,r}(0.0) = [-0.19, -0.42, -0.75],$$
$$K^{[0.1,0.3,0.5]}_{\odot,z}(0.0) = [-0.08, -0.26, -0.33].$$

Apart from the k-corrections, Blanton & Roweis (2007) also provide an estimation of the stellar mass for each galaxy with fast spectral analysis and stellar composition estimation. They combine heterogeneous data (including broadband fluxes at various redshifts) in order to determine the properties of the subspace of galaxy spectra. They restrict the space of possible spectra to those predicted from the high-resolution stellar population synthesis model of Bruzual & Charlot (2003) and the nebular emission line models of Kewley et al. (2001). This approach yields a natural theoretical interpretation of the results in terms of star formation histories. The consistency of this method with the mass-to-light ratio method proposed by Kauffmann et al. (2003) has been checked and verified. However, due to the limitations of redshift uncertainty and the templates used, the stellar masses obtained by the k-correction code should be handled with caution. The stellar masses may be overestimated to some extent due to the long star formation

Table 2
Mean k-corrections for r and z Bands across Various Galaxy Color Categories (Four Color Bins) over Three Redshift Ranges

		0.0–0.2			0.2–0.4			0.4–0.6		
		a_μ	b_μ	c_μ	a_μ	b_μ	c_μ	a_μ	b_μ	c_μ
r band	Color $\mu = 1$ (blue)	−4.72	1.48	−0.22	1.06	−0.49	−0.24	−0.50	1.60	−1.12
	Color $\mu = 2$	−1.52	0.98	−0.19	1.57	−0.24	−0.36	3.41	−1.30	−0.64
	Color $\mu = 3$	0.40	0.78	−0.19	2.60	−0.24	−0.45	4.29	−1.28	−0.88
	Color $\mu = 4$ (red)	1.10	0.78	−0.19	2.27	0.22	−0.55	3.62	−0.55	−1.08
	Total	0.13	0.80	−0.19	2.35	−0.21	−0.43	1.16	1.32	−1.40
z band	Color $\mu = 1$ (blue)	0.89	−0.41	−0.07	0.68	−0.90	−0.04	2.60	−2.00	−0.08
	Color $\mu = 2$	1.93	−0.51	−0.07	0.70	−0.46	−0.20	2.65	−2.00	−0.10
	Color $\mu = 3$	1.97	−0.33	−0.09	0.70	−0.05	−0.33	1.72	−1.11	−0.31
	Color $\mu = 4$ (red)	1.35	−0.07	−0.11	0.21	0.42	−0.42	1.65	−0.99	−0.35
	Total	2.24	−0.45	−0.08	0.82	−0.17	−0.30	1.82	−1.19	−0.29

history assumed, particularly at high redshifts. Nevertheless, it still provides a quick and efficient estimation of the stellar mass. Furthermore, we have also adopted the spectral energy distribution (SED) code CIGALE (Boquien 2020), which is an alternative method for estimating stellar mass and is applied to DESI observations in Xu et al. (2022). The stellar masses derived using CIGALE align with our results, maintaining consistency within a margin of error of 0.1 dex across various stellar mass scales.

3. The Impact of Photo-z Errors on the LF and SMF Measurements

Prior to examining the CLF and CSMF, this section will analyze the impact of photo-z errors on the measurements of LFs and SMFs using the Y1-BGS and SV3-BGS subsamples.

3.1. Galaxy LFs

We employ a standard $V_{\rm max}$ approach to calculate the LFs for the r band and z band. We start by removing any galaxies with apparent magnitudes beyond the magnitude limit from a magnitude-limited galaxy sample ($m_r \leqslant 19.5$ and $m_z \leqslant 19$). We then select the redshift range $[z_1, z_2]$ within which the galaxies are used for the LF measurements. For a galaxy with a specific absolute magnitude, we determine the maximum redshift $z_{\rm max}$ below which the galaxy can be observed by adopting an approximate k-correction in this process. Finally, we calculate the effective volume for the galaxy according to the redshift range $[z_1, \min(z_2, z_{\rm max})]$.

In general, the approximate k-correction applied to calculate $z_{\rm max}$ can be described as

$$M^j{}_X - 5\log h = m_X^{\rm limit} - {\rm DM}(z_{\rm max}) - K'^j{}_X(z_{\rm max}), \quad (4)$$

where $m_X^{\rm limit}$ is the magnitude limit, 19.5 for the r band and 19 for the z band, and

$$K'^j{}_X(z_{\rm max}) = K^j_X(z_{\rm obs}) + \bar{K}^j_X(z_{\rm max}) - \bar{K}^j_X(z_{\rm obs}) \quad (5)$$

is an approximate k-correction when relocating a galaxy at $z_{\rm obs}$ to $z_{\rm max}$, which can be estimated by the mean k-correction as a function of galaxy color and redshift at these two redshifts,

$$\bar{K}^j_X(z) = \Sigma\ \omega_\mu (r - z)(a_\mu z^2 + b_\mu z + c_\mu). \quad (6)$$

Following Rodriguez-Puebla et al. (2020), galaxies within each redshift bin are initially categorized into four $r - z$ color bins indicating by μ, and the weight ω_μ is determined with the distance of a given galaxy to the bin center on the color–magnitude plane. The redshift-dependent coefficients a_μ, b_μ, and c_μ for the mean k-correction in each color bin μ are derived by fitting the k-correction from Blanton & Roweis (2007), and the results are shown in Table 2. The k-correction, $K'^j_X(z_{\rm max})$, is then applied to determine the corresponding $z_{\rm max}$.

To ensure the quality of observation data, we calculated the fraction $f_{\rm comp}(m_z)$, which represents the ratio of the number of galaxies with observations at five wavelengths to the number of all galaxies, using healpix (Górski et al. 2005) as a function of the apparent magnitude of the z band and the color of the galaxy in each pixel. This factor is then used to adjust for the selection incompleteness in the subsequent analysis.

We first measure the LFs of the Y1-BGS (Y1-r19.5 or Y1-z19.0) and SV3-BGS (SV3-r19.5 or SV3-z19.0) subsamples in three redshift bins. The upper and middle panels of Figure 2 show the results for the r and z bands, respectively. The LFs of the two bands are generally consistent, although the r-band luminosity is slightly lower than the z-band luminosity. The blue dots with error bars represent the SV3-BGS subsample, which has a small sky coverage (133 deg^2) and most of the galaxies with spectroscopic redshifts, thus providing the most reliable LF measurements. The magenta dots show the results of the Y1-BGS subsample, which has a large sky coverage (12,276 deg^2) and has roughly half of its galaxies with spectroscopic redshifts. Overall, the LFs of Y1-BGS and SV3-BGS show very good agreement with each other with negligible differences in all redshift bins. The main deviations from the SV3-BGS subsample only become prominent as the luminosity decreases below $L \leqslant 10^{8.5}\, h^{-2}\, L_\odot$.

To investigate the influence of photo-z errors on LF measurements, we created a degraded SV3-BGS sample (spectral percentage of galaxies ∼45%, hereafter spec ∼45%) which closely matches the spectral completeness of Y1-BGS by randomly replacing 55% of the spectroscopic redshifts of the galaxies with their original photometric redshifts before obtaining the spectroscopic observation of SV3-BGS and showing the results with green dots. The error bars are estimated using the bootstrap method, which randomly resamples the original galaxy sample with replacement while keeping the total number of galaxies unchanged. To demonstrate the deviations more clearly, the logarithmic differences between the LFs of Y1-BGS (spec ∼45%) and SV3-BGS are shown in the lower part of each panel in Figure 2. The degraded SV3-BGS and Y1-BGS subsamples show good agreement within 1σ, demonstrating that the differences

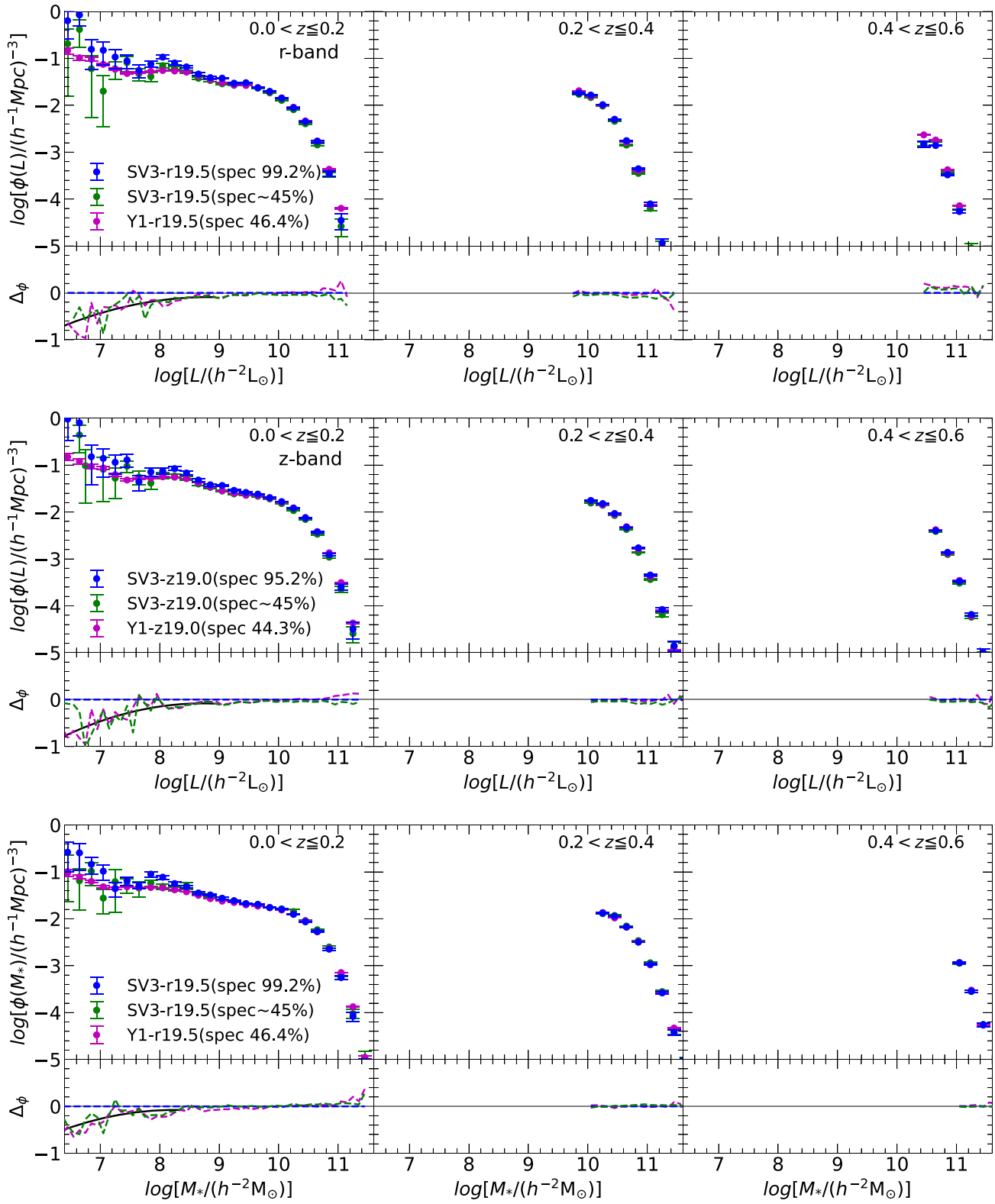

Figure 2. Galaxy LFs and SMFs in three redshift bins as indicated for two observational subsamples after k-correction. The upper, middle, and lower panels show the results for r-band luminosity, z-band luminosity, and stellar mass, respectively. The blue and magenta dots in each panel are for the SV3-r19.5 (SV3-z19.0) and Y1-r19.5 (Y1-z19.0) subsamples, respectively. The green ones are the results of a degraded SV3-BGS (spec ∼45%) subsample. The error bars are obtained from the standard deviation of 200 bootstrap resamplings. The lower portions of the panels show deviations between SV3-BGS and other samples. The black solid lines are the fitting formulae of the suppression factors, which are $-0.103(\log L)^2 + 1.815(\log L) - 8.100$, $-0.130(\log L)^2 + 2.258(\log L) - 9.925$, and $-0.123(\log M_*)^2 + 2.027(\log M_*) - 8.425$, for the upper, middle, and lower panels, respectively.

between the SV3-BGS and Y1-BGS results are indeed caused by the photo-z error.

We use a quadratic function (represented by the solid black curves) to fit the deviation of LFs from the original to degraded SV3-BGS subsamples, which will be used to correct the LF deviations observed in the Y1-BGS subsamples. The fitted deviations for the r band and z band are $-0.103(\log L)^2 + 1.815(\log L) - 8.100$ and $-0.130(\log L)^2 + 2.258(\log L) - 9.925$, respectively. To avoid overcrowding of LF and SMF data points, only half of the luminosity bins listed in Table 3 are shown. For $\Delta\phi$, all luminosity bins are shown with dashed lines.

3.2. Galaxy SMFs

The stellar mass of galaxies is one of the most important properties in the study of galaxy evolution and cosmic structure evolution. It can be reliably measured using SED modeling (Conroy et al. 2009; Conroy 2013; Song et al. 2023) and is more commonly used in theoretical studies. In measuring the galaxy SMFs, we use the r-band apparent and absolute magnitudes to calculate $z_{\max}$ for each galaxy in our SV3-r19.5 and Y1-r19.5 subsamples. The resulting SMFs are shown in the lower panels of Figure 2. As we have tested, the SMFs of SV3-BGS and Y1-BGS using the CIGALE and k-correction code are in good agreement with each other within 1σ error bars.

These SMFs display similar trends to the LFs, especially the enhancement starting around $M_* \sim 10^{8.5}\,h^{-2}\,M_\odot$. This kind of enhancement in SMFs at the low-mass end was also reported in a recent study carried out by Gao et al. (2023). Finally, similar to the LFs, we also fit the deviation of SMFs of the degraded SV3-BGS (spec ∼45%) subsample with respect to the initial SV3-BGS subsample using a quadratic function form, denoted by the solid black lines in Figure 2. This fitting result, $-0.123(\log M_*)^2 + 2.027(\log M_*) - 8.425$, can be applied to correct the SMF suppression of Y1-BGS at the low-mass end. The results of the LFs and SMFs obtained from SV3-BGS are provided in Table 3 for reference.

4. Testing the Reliability of CLF Measurements Using MGRS

Due to various selection effects, observational data sometimes might lead to biased measurements. To assess the influence of the group finder and photo-z error on the CLF and CSMF measurements, we create an MGRS from the Jiutian simulation with the same sky coverage as the LS DR9. The luminosity of the MGRS is adjusted to match the z-band LFs from the Y1-z19.0 sample after a correction factor is applied to the SV3-z19.0 sample. Two sets of mock group catalogs are then generated from the MGRS using the extended halo-based group finder with either spectroscopic or photometric redshifts.

4.1. Constructing an MGRS from the Jiutian Simulation

We employed a high-resolution dark-matter-only N-body simulation from the Jiutian simulation suite, specifically designed for the optical surveys conducted by the Chinese Space-station Survey Telescope (Zhan 2011, 2018), to construct our MGRS (Gu et al. 2024). The three main runs of the simulation suite are based on Planck 2018 cosmology (Planck Collaboration et al. 2020), with parameters listed in Section 1, evolving 6144^3 particles in boxes of 0.3, 1, and 2 Gpc h^{-1} on a side. Extension runs spanning various cosmologies and constrained runs reproducing the large-scale structure in the observation will also be available. The simulation we adopted is the main run of 1 Gpc h^{-1} with a particle mass of $m_p = 3.723 \times 10^8\,h^{-1}\,M_\odot$ using the GADGET-3 code (Springel et al. 2001; Springel 2005). The simulation began at an initial redshift of 127, producing 128 snapshots to $z = 0$. The friends-of-friends algorithm (Davis et al. 1985) with a linking length of 0.2 times the mean interparticle separation was used to identify dark matter halos. The HBT+ code (Han et al. 2012, 2018)[41] was then used to identify subhalos and their evolution histories.

An observer is placed at a reference location in the box, and each snapshot is replicated periodically to create a subhalo light cone. The orbit of each subhalo is then interpolated over time to determine the time and location at which the subhalo should be observed. The properties of the subhalo are then interpolated to the intersecting time to generate a light-cone catalog of subhalos. This method allows for the precise recovery of the mass function and clustering of (sub)halos across different redshifts. Furthermore, the large size of our simulation box minimizes the duplication of subhalos, particularly at lower redshifts. Using the Jiutian subhalo light-cone catalog, we assign a z-band galaxy luminosity to each subhalo with SHAM (Vale & Ostriker 2004; Reddick et al. 2013) that incorporates a luminosity scatter $\sigma_{\log L} = 0.15$ dex at a fixed subhalo mass. The subhalo mass we adopted is the maximum mass along the accretion history. The cumulative LFs used for the abundance matching are directly measured from the Y1-z19.0 sample with narrow redshift bins. To assign luminosity to each subhalo at a particular redshift, we interpolated the LFs at different redshifts. It is worth noting that $V_{\rm peak}$ may be more preferred than the peak mass as a subhalo mass indicator for SHAM in the literature (Reddick et al. 2013; Lehmann et al. 2017; Dragomir et al. 2018), and the comparison of the two will be discussed in more detail in a forthcoming paper (H. J. Xu et al. 2024, in preparation).

Our MGRS for LS DR9 is constructed by ensuring that it covers the same area as LS DR9, with a magnitude limit of $m_z \leqslant 21.0$ and a redshift interval of [0.0, 1.0]. Additionally, we apply bright-star masking to the MGRS. Relative to the original north galactic cap of the MGRS, the galaxy count postmasking decreases by 2.8 million, and the sky coverage shrinks by 476 deg^2. Figure 3 displays the LFs from our MGRS (MGRS-simu, depicted as dark brown open circles with error bars) alongside the observational data from Y1-z19.0 (magenta) and SV3-z19.0 (blue), showing a good match, which is anticipated due to the use of the abundance matching technique.

In order to account for observational effects in redshift measurements, two additional redshifts are assigned to each galaxy in addition to the true MGRS-simu. The first of these is the MGRS-spec, which takes into account the redshift error of the DESI spectroscopic observation at about 35 km s^{-1} and the peculiar velocity of the galaxy. The other is the MGRS-photo, which includes a photo-z error with a Gaussian distribution as described in Yang et al. (2021), $\sigma_z = (0.01 + 0.015z)^*(1 + z)$. To best mimic Y1-BGS, for galaxies with $m_z < 19.0$, we randomly choose 45% of them to keep the spectroscopic redshifts.

The light brown and orange open circles in Figure 3 represent the LFs obtained from the MGRS-spec and MGRS-

[41] https://github.com/Kambrian/HBTplus

Table 3
Values of the Galaxy LFs and SMFs Obtained from SV3-r19.5 and SV3-z19.0 Subsamples in Different Redshift Bins

L or M_* $[h^{-2}\,L_\odot]$ $[h^{-2}\,M_\odot]$	$\log\Phi(L)$ − r band $[h^3\,\mathrm{Mpc}^{-3}\,d\log L]$			$\log\Phi(L)$ − z band $[h^3\,\mathrm{Mpc}^{-3}\,d\log L]$			$\log\Phi(M_*)$ $[h^3\,\mathrm{Mpc}^{-3}\,d\log M_*]$		
	0.0–0.2	0.2–0.4	0.4–0.6	0.0–0.2	0.2–0.4	0.4–0.6	0.0–0.2	0.2–0.4	0.4–0.6
6.45	$-0.1967^{+0.2028}_{-0.3927}$	⋯	⋯	$-0.0186^{+0.2175}_{-0.4561}$	⋯	⋯	$-0.5806^{+0.2088}_{-0.4174}$	⋯	⋯
6.55	$-0.0175^{+0.1364}_{-0.2001}$	⋯	⋯	$-0.1533^{+0.2098}_{-0.4216}$	⋯	⋯	$-0.3140^{+0.1889}_{-0.3421}$	⋯	⋯
6.65	$-0.0737^{+0.1540}_{-0.2408}$	⋯	⋯	$-0.0981^{+0.1682}_{-0.2782}$	⋯	⋯	$-0.5941^{+0.1983}_{-0.3756}$	⋯	⋯
6.75	$-0.0670^{+0.1165}_{-0.1597}$	⋯	⋯	$0.00546^{+0.1414}_{-0.2111}$	⋯	⋯	$-0.5580^{+0.1798}_{-0.3123}$	⋯	⋯
6.85	$-0.8062^{+0.2105}_{-0.4245}$	⋯	⋯	$-0.8216^{+0.2432}_{-0.6036}$	⋯	⋯	$-0.8368^{+0.1394}_{-0.2065}$	⋯	⋯
6.95	$-0.4230^{+0.1301}_{-0.1866}$	⋯	⋯	$-0.3453^{+0.1331}_{-0.1930}$	⋯	⋯	$-0.8681^{+0.1563}_{-0.2465}$	⋯	⋯
7.05	$-0.8264^{+0.1814}_{-0.3174}$	⋯	⋯	$-0.8552^{+0.2046}_{-0.3999}$	⋯	⋯	$-0.9860^{+0.1298}_{-0.1861}$	⋯	⋯
7.15	$-0.8980^{+0.1510}_{-0.2335}$	⋯	⋯	$-0.6113^{+0.1520}_{-0.2360}$	⋯	⋯	$-1.1888^{+0.1300}_{-0.1864}$	⋯	⋯
7.25	$-0.9709^{+0.1588}_{-0.2530}$	⋯	⋯	$-0.9390^{+0.1594}_{-0.2546}$	⋯	⋯	$-1.3580^{+0.1302}_{-0.1868}$	⋯	⋯
7.35	$-0.9116^{+0.1321}_{-0.1908}$	⋯	⋯	$-0.8751^{+0.1332}_{-0.1931}$	⋯	⋯	$-1.2177^{+0.1197}_{-0.1659}$	⋯	⋯
7.45	$-1.0523^{+0.1193}_{-0.1650}$	⋯	⋯	$-0.8890^{+0.1142}_{-0.1554}$	⋯	⋯	$-1.1906^{+0.0814}_{-0.1003}$	⋯	⋯
7.55	$-1.3414^{+0.1388}_{-0.2053}$	⋯	⋯	$-1.1349^{+0.1348}_{-0.1966}$	⋯	⋯	$-1.2387^{+0.0826}_{-0.1021}$	⋯	⋯
7.65	$-1.2584^{+0.1173}_{-0.1613}$	⋯	⋯	$-1.3557^{+0.1318}_{-0.1902}$	⋯	⋯	$-1.2919^{+0.0588}_{-0.0680}$	⋯	⋯
7.75	$-1.0426^{+0.0614}_{-0.0716}$	⋯	⋯	$-1.2047^{+0.1004}_{-0.1309}$	⋯	⋯	$-1.1429^{+0.0549}_{-0.0629}$	⋯	⋯
7.85	$-1.1208^{+0.0608}_{-0.0707}$	⋯	⋯	$-1.1441^{+0.0806}_{-0.0990}$	⋯	⋯	$-1.0476^{+0.0529}_{-0.0602}$	⋯	⋯
7.95	$-1.1091^{+0.0560}_{-0.0643}$	⋯	⋯	$-1.3577^{+0.0859}_{-0.1073}$	⋯	⋯	$-1.1211^{+0.0457}_{-0.0511}$	⋯	⋯
8.05	$-0.9730^{+0.0387}_{-0.0425}$	⋯	⋯	$-1.1244^{+0.0603}_{-0.0700}$	⋯	⋯	$-1.1136^{+0.0379}_{-0.0416}$	⋯	⋯
8.15	$-1.0043^{+0.0402}_{-0.0443}$	⋯	⋯	$-1.0548^{+0.0489}_{-0.0551}$	⋯	⋯	$-1.1513^{+0.0334}_{-0.0362}$	⋯	⋯
8.25	$-1.0976^{+0.0341}_{-0.0370}$	⋯	⋯	$-1.0740^{+0.0398}_{-0.0438}$	⋯	⋯	$-1.2495^{+0.0360}_{-0.0393}$	⋯	⋯
8.35	$-1.1191^{+0.0311}_{-0.0335}$	⋯	⋯	$-1.0818^{+0.0348}_{-0.0378}$	⋯	⋯	$-1.3290^{+0.0334}_{-0.0362}$	⋯	⋯
8.45	$-1.1817^{+0.0271}_{-0.0289}$	⋯	⋯	$-1.1681^{+0.0357}_{-0.0389}$	⋯	⋯	$-1.3157^{+0.0307}_{-0.0330}$	⋯	⋯
8.55	$-1.2463^{+0.0247}_{-0.0262}$	⋯	⋯	$-1.2526^{+0.0301}_{-0.0323}$	⋯	⋯	$-1.4163^{+0.0293}_{-0.0314}$	⋯	⋯
8.65	$-1.3337^{+0.0264}_{-0.0281}$	⋯	⋯	$-1.3174^{+0.0275}_{-0.0293}$	⋯	⋯	$-1.4494^{+0.0264}_{-0.0281}$	⋯	⋯
8.75	$-1.3414^{+0.0215}_{-0.0227}$	⋯	⋯	$-1.3747^{+0.0261}_{-0.0278}$	⋯	⋯	$-1.4216^{+0.0241}_{-0.0255}$	⋯	⋯
8.85	$-1.4107^{+0.0195}_{-0.0205}$	⋯	⋯	$-1.4189^{+0.0236}_{-0.0250}$	⋯	⋯	$-1.4911^{+0.0195}_{-0.0204}$	⋯	⋯
8.95	$-1.3755^{+0.0131}_{-0.0135}$	⋯	⋯	$-1.4706^{+0.0207}_{-0.0217}$	⋯	⋯	$-1.5238^{+0.0168}_{-0.0175}$	⋯	⋯
9.05	$-1.4224^{+0.0142}_{-0.0147}$	⋯	⋯	$-1.4340^{+0.0139}_{-0.0143}$	⋯	⋯	$-1.5626^{+0.0190}_{-0.0199}$	⋯	⋯
9.15	$-1.4838^{+0.0130}_{-0.0134}$	⋯	⋯	$-1.4839^{+0.0151}_{-0.0156}$	⋯	⋯	$-1.5694^{+0.0157}_{-0.0163}$	⋯	⋯
9.25	$-1.5282^{+0.0113}_{-0.0116}$	⋯	⋯	$-1.5382^{+0.0137}_{-0.0141}$	⋯	⋯	$-1.6140^{+0.0145}_{-0.0150}$	⋯	⋯
9.35	$-1.5252^{+0.0090}_{-0.0092}$	⋯	⋯	$-1.5743^{+0.0122}_{-0.0125}$	⋯	⋯	$-1.6170^{+0.0129}_{-0.0133}$	⋯	⋯
9.45	$-1.5195^{+0.0094}_{-0.0096}$	⋯	⋯	$-1.5824^{+0.0104}_{-0.0107}$	⋯	⋯	$-1.6761^{+0.0119}_{-0.0122}$	⋯	⋯
9.55	$-1.5771^{+0.0076}_{-0.0078}$	⋯	⋯	$-1.5641^{+0.0088}_{-0.0090}$	⋯	⋯	$-1.6597^{+0.0106}_{-0.0109}$	⋯	⋯
9.65	$-1.6260^{+0.0075}_{-0.0076}$	⋯	⋯	$-1.6177^{+0.0082}_{-0.0083}$	⋯	⋯	$-1.6916^{+0.0091}_{-0.0093}$	⋯	⋯
9.75	$-1.6443^{+0.0068}_{-0.0069}$	⋯	⋯	$-1.6675^{+0.0071}_{-0.0072}$	⋯	⋯	$-1.7008^{+0.0088}_{-0.0090}$	⋯	⋯
9.85	$-1.7039^{+0.0062}_{-0.0063}$	$-1.7373^{+0.0145}_{-0.0150}$	⋯	$-1.6927^{+0.0057}_{-0.0058}$	⋯	⋯	$-1.7598^{+0.0081}_{-0.0082}$	⋯	⋯
9.95	$-1.7649^{+0.0064}_{-0.0065}$	$-1.7571^{+0.0074}_{-0.0076}$	⋯	$-1.7187^{+0.0062}_{-0.0063}$	$-1.7403^{+0.0148}_{-0.0153}$	⋯	$-1.7736^{+0.0092}_{-0.0094}$	⋯	⋯
10.05	$-1.8477^{+0.0076}_{-0.0077}$	$-1.7825^{+0.0061}_{-0.0062}$	⋯	$-1.7778^{+0.0070}_{-0.0071}$	$-1.7549^{+0.0086}_{-0.0088}$	⋯	$-1.7950^{+0.0060}_{-0.0061}$	⋯	⋯
10.15	$-1.9458^{+0.0083}_{-0.0085}$	$-1.8634^{+0.0054}_{-0.0054}$	⋯	$-1.8437^{+0.0065}_{-0.0066}$	$-1.7721^{+0.0060}_{-0.0061}$	⋯	$-1.8548^{+0.0075}_{-0.0076}$	$-1.8597^{+0.0150}_{-0.0155}$	⋯
10.25	$-2.0531^{+0.0104}_{-0.0106}$	$-1.9878^{+0.0052}_{-0.0053}$	⋯	$-1.9164^{+0.0073}_{-0.0074}$	$-1.8201^{+0.0048}_{-0.0049}$	⋯	$-1.9053^{+0.0082}_{-0.0084}$	$-1.8782^{+0.0100}_{-0.0102}$	⋯
10.35	$-2.1708^{+0.0117}_{-0.0120}$	$-2.1360^{+0.0056}_{-0.0056}$	⋯	$-2.0191^{+0.0093}_{-0.0096}$	$-1.9171^{+0.0045}_{-0.0046}$	⋯	$-1.9751^{+0.0098}_{-0.0100}$	$-1.9156^{+0.0074}_{-0.0075}$	⋯
10.45	$-2.3505^{+0.0140}_{-0.0145}$	$-2.3025^{+0.0059}_{-0.0060}$	⋯	$-2.1249^{+0.0105}_{-0.0107}$	$-2.0319^{+0.0045}_{-0.0045}$	⋯	$-2.0641^{+0.0100}_{-0.0102}$	$-1.9441^{+0.0062}_{-0.0063}$	⋯

Table 3
(Continued)

L or M_* $[h^{-2}\ L_\odot]$ $[h^{-2}\ M_\odot]$	$\log\Phi(L)$ − r band $[h^3\ \mathrm{Mpc}^{-3}\ d\log L]$			$\log\Phi(L)$ − z band $[h^3\ \mathrm{Mpc}^{-3}\ d\log L]$			$\log\Phi(M_*)$ $[h^3\ \mathrm{Mpc}^{-3}\ d\log M_*]$		
	0.0–0.2	0.2–0.4	0.4–0.6	0.0–0.2	0.2–0.4	0.4–0.6	0.0–0.2	0.2–0.4	0.4–0.6
10.55	$-2.5483^{+0.0173}_{-0.0180}$	$-2.5129^{+0.0068}_{-0.0069}$	$-2.6235^{+0.0163}_{-0.0169}$	$-2.2473^{+0.0121}_{-0.0124}$	$-2.1759^{+0.0043}_{-0.0043}$	$-2.2477^{+0.0181}_{-0.0189}$	$-2.1691^{+0.0115}_{-0.0118}$	$-2.0596^{+0.0059}_{-0.0059}$	⋯
10.65	$-2.7684^{+0.0226}_{-0.0239}$	$-2.7542^{+0.0087}_{-0.0089}$	$-2.8579^{+0.0129}_{-0.0133}$	$-2.4249^{+0.0137}_{-0.0142}$	$-2.3303^{+0.0051}_{-0.0052}$	$-2.3964^{+0.0074}_{-0.0076}$	$-2.2714^{+0.0122}_{-0.0125}$	$-2.1738^{+0.0066}_{-0.0067}$	⋯
10.75	$-3.1338^{+0.0356}_{-0.0387}$	$-3.0326^{+0.0115}_{-0.0119}$	$-3.1627^{+0.0139}_{-0.0144}$	$-2.6385^{+0.0199}_{-0.0209}$	$-2.5196^{+0.0064}_{-0.0065}$	$-2.6203^{+0.0071}_{-0.0072}$	$-2.4683^{+0.0166}_{-0.0172}$	$-2.3222^{+0.0058}_{-0.0059}$	⋯
10.85	$-3.4533^{+0.0498}_{-0.0563}$	$-3.3540^{+0.0176}_{-0.0183}$	$-3.4830^{+0.0211}_{-0.0222}$	$-2.9081^{+0.0236}_{-0.0250}$	$-2.7634^{+0.0111}_{-0.0114}$	$-2.8605^{+0.0073}_{-0.0075}$	$-2.6473^{+0.0210}_{-0.0221}$	$-2.4985^{+0.0068}_{-0.0069}$	⋯
10.95	$-3.8053^{+0.0708}_{-0.0846}$	$-3.7260^{+0.0262}_{-0.0279}$	$-3.8880^{+0.0257}_{-0.0273}$	$-3.2384^{+0.0364}_{-0.0397}$	$-3.0322^{+0.0120}_{-0.0123}$	$-3.1485^{+0.0093}_{-0.0096}$	$-2.8964^{+0.0248}_{-0.0263}$	$-2.7192^{+0.0087}_{-0.0089}$	$-2.7514^{+0.0324}_{-0.0350}$
11.05	$-4.4542^{+0.1397}_{-0.2073}$	$-4.1033^{+0.0364}_{-0.0398}$	$-4.2659^{+0.0356}_{-0.0388}$	$-3.5929^{+0.0570}_{-0.0657}$	$-3.3436^{+0.0184}_{-0.0192}$	$-3.4799^{+0.0128}_{-0.0132}$	$-3.2529^{+0.0388}_{-0.0427}$	$-2.9692^{+0.0107}_{-0.0110}$	$-2.9404^{+0.0147}_{-0.0152}$
11.15	$-4.6842^{+0.1602}_{-0.2565}$	$-4.6675^{+0.0787}_{-0.0962}$	$-4.7231^{+0.0567}_{-0.0653}$	$-4.0093^{+0.0910}_{-0.1153}$	$-3.7102^{+0.0239}_{-0.0253}$	$-3.7984^{+0.0215}_{-0.0226}$	$-3.5683^{+0.0510}_{-0.0579}$	$-3.2492^{+0.0148}_{-0.0153}$	$-3.2121^{+0.0234}_{-0.0247}$
11.25	⋯	$-4.9351^{+0.0912}_{-0.1156}$	$-5.1914^{+0.0906}_{-0.1146}$	$-4.4976^{+0.1417}_{-0.2117}$	$-4.0792^{+0.0402}_{-0.0443}$	$-4.1849^{+0.0303}_{-0.0326}$	$-4.0808^{+0.0871}_{-0.1091}$	$-3.5797^{+0.0242}_{-0.0256}$	$-3.5444^{+0.0212}_{-0.0223}$
11.35	⋯	$-5.4608^{+0.1745}_{-0.2963}$	$-5.4673^{+0.1267}_{-0.1798}$	$-5.0903^{+0.2440}_{-0.6093}$	$-4.6180^{+0.0677}_{-0.0803}$	$-4.7458^{+0.0571}_{-0.0657}$	$-4.4571^{+0.1444}_{-0.2180}$	$-3.9017^{+0.0372}_{-0.0407}$	$-3.9025^{+0.0256}_{-0.0272}$
11.45	⋯	$-5.8772^{+0.2265}_{-0.5012}$	$-6.1826^{+0.2603}_{-0.7476}$	⋯	$-4.8526^{+0.0925}_{-0.1177}$	$-4.9955^{+0.0747}_{-0.0902}$	$-5.3309^{+0.3430}_{-0.6926}$	$-4.4195^{+0.0548}_{-0.0627}$	$-4.2583^{+0.0417}_{-0.0462}$
11.55	⋯	⋯	⋯	⋯	$-5.5604^{+0.1891}_{-0.3428}$	$-5.4857^{+0.1211}_{-0.1686}$	⋯	$-4.8287^{+0.0790}_{-0.0967}$	$-4.7906^{+0.0566}_{-0.0651}$
11.65	⋯	⋯	$-6.4058^{+0.3149}_{-1.1864}$	⋯	$-5.8315^{+0.2558}_{-0.7039}$	$-6.5010^{+0.3086}_{-1.4491}$	⋯	$-5.0822^{+0.1102}_{-0.1480}$	$-5.2429^{+0.1055}_{-0.1397}$
11.75	⋯	⋯	⋯	⋯	⋯	$-6.4879^{+0.2898}_{-1.2941}$	⋯	$-5.5104^{+0.1841}_{-0.3261}$	$-5.8058^{+0.1655}_{-0.2709}$

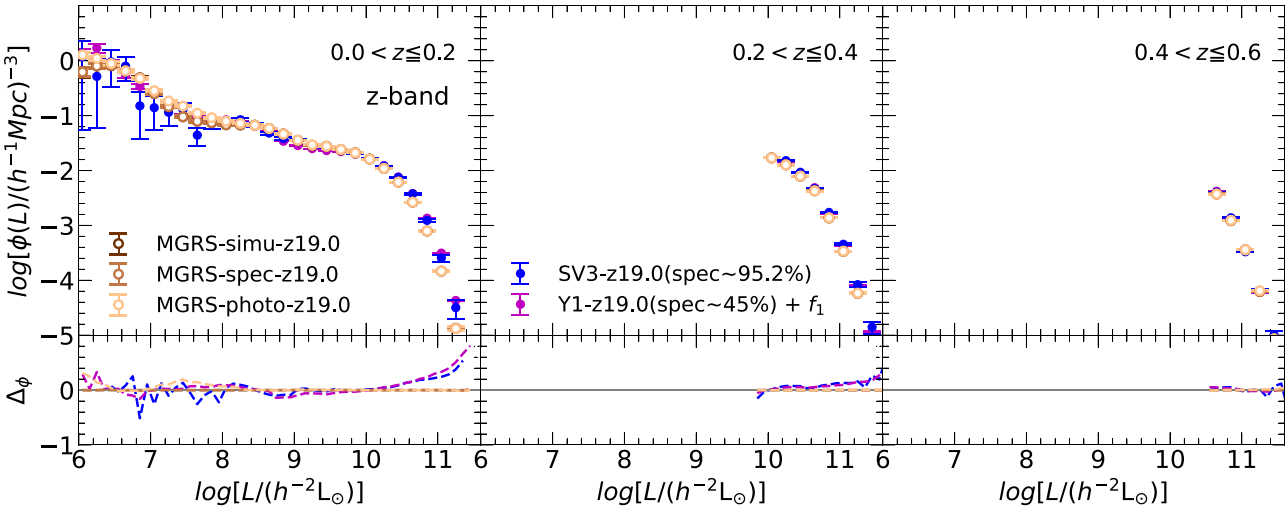

Figure 3. LFs (z band) of the DESI LS DR9 MGRS. Here MGRS-simu (dark brown), MGRS-spec (light brown), and MGRS-photo (orange) represent mock galaxies in real space, with spectroscopic redshifts and mixed spectroscopic and photometric redshifts, respectively. Also, we show LFs of observations (SV3-z19.0 and Y1-z19.0) for comparison. MGRS-simu and MGRS-spec are virtually indistinguishable. The error bars are obtained from the standard deviation of 200 bootstrap resamplings. The lower panels show deviations between MGRS-simu-z19.0 and other samples.

photo, respectively. All measurements based on the MGRS agree, even for luminosities of $L \sim 10^6\ h^{-1}\ L_\odot$. The MGRS-simu and MGRS-spec are almost indistinguishable in all redshift bins, while the MGRS-photo displays a slightly smoother trend at the faint end in the lowest redshift bin, which is caused by the Gaussian photo-z error we applied. The behavior of MGRS-photo suggests that a pure Gaussian photo error cannot accurately reproduce the decreasing behavior of the observed LFs of the half-spectroscopic sample at the faint end, as seen in Figure 2.

To delve deeper into the cause of the decline in LFs at the faint end due to the actual photo-z distributions observed in the DESI LS, we examine the redshift distribution of galaxies with an apparent magnitude of $18.5 < r < 19.5$, as the faint-end LFs are mainly contributed by these galaxies. As depicted in Figure B1 in Appendix B, in comparison to the spectroscopic redshift distribution, galaxies in the lowest redshift peak at approximately $z = 0$ exhibit a non-Gaussian photo-z distribution. Specifically, their photo-z distribution leans toward higher redshifts. Consequently, the observed decrease in the LFs/SMFs in the DESI data is primarily due to the skewed nature of the photo-z in the LS DR9.

4.2. Comparing the True and Measured CLFs

The CLF describes the average number of galaxies as a function of galaxy luminosity in the dark matter halo of a given mass, which plays an essential role in understanding how galaxies form and distribute in dark matter halos. In this subsection, we assess the impact of the group finder on the CLF measurements by comparing the results from MGRS-spec and MGRS-photo to the true input values (MGRS-simu). To do this, we apply the same extended group finder from Yang et al. (2021) to identify groups in our LS DR9 MGRS. We then construct two versions of mock group catalogs, one for MGRS-spec and the other for MGRS-photo. We used MGRS-spec, MGRS-photo, and MGRS-simu to represent the results measured from the two mock group catalogs and the true input values, respectively.

The CLF is measured differently from the LF, which is normalized by the number of groups in the redshift range instead of the cosmic volume. The same critical step of determining the maximum redshift $z_{\rm max}$ is still necessary. To calculate the CLF, galaxies and groups in the redshift range [z_1, z_2] are first selected. For a galaxy with a specific absolute magnitude, the maximum redshift $z_{\rm max}$ is then determined. The effective number of groups is calculated by counting the number of groups within the redshift range [z_1, min(z_2, $z_{\rm max}$)]. Figure 4 shows the CLFs in the z band obtained from the Jiutian MGRS in different halo mass and redshift bins. The redshift range is from [0.0, 0.2], [0.2, 0.4], and [0.4, 0.6] from the top to bottom panels. The halo mass bins are [$10^{14.4}$, $10^{14.7}$], [$10^{13.5}$, $10^{13.8}$], [$10^{12.9}$, $10^{13.2}$], and [$10^{12.0}$, $10^{12.3}$] (units of $h^{-1}\ M_\odot$) from left to right.

We find that the central galaxy CLFs in both MGRS-spec and MGRS-photo are accurately reproduced in halos with masses greater than $10^{13}\ h^{-1}\ M_\odot$, regardless of redshift. The median values of these samples are similar to those of MGRS-simu in less massive halos; however, the scatter is slightly underestimated due to the estimation of the halo mass based on abundance matching (Yang et al. 2005b). Xu et al. (2023) recently reported that the group finder could create an artificial double-peak profile in the central CLF for a shallow survey. They found that the brighter component of the double peak is largely contributed by the groups with a single member galaxy (see Appendix A for a more detailed discussion). Such artifacts can be greatly reduced by using a deeper survey. We do not observe this feature, which manifests the validation of using a deeper survey for the group-finding process. In summary, the CLFs for central galaxies in DESI DR9 can be well recovered, except for scatter in small halos.

The CLFs of satellites derived from the MGRS-spec, MGRS-photo, and MGRS-simu samples with luminosity greater than $10^8\ h^{-2}\ L_\odot$ also show very good agreement within different halo mass bins and redshift ranges. Most of the data points agree well with each other within their 1σ error bars. The only slight difference we can see is in the lowest halo mass bin, where the CLF from MGRS-spec tends to be slightly underestimated compared to MGRS-simu, with a difference

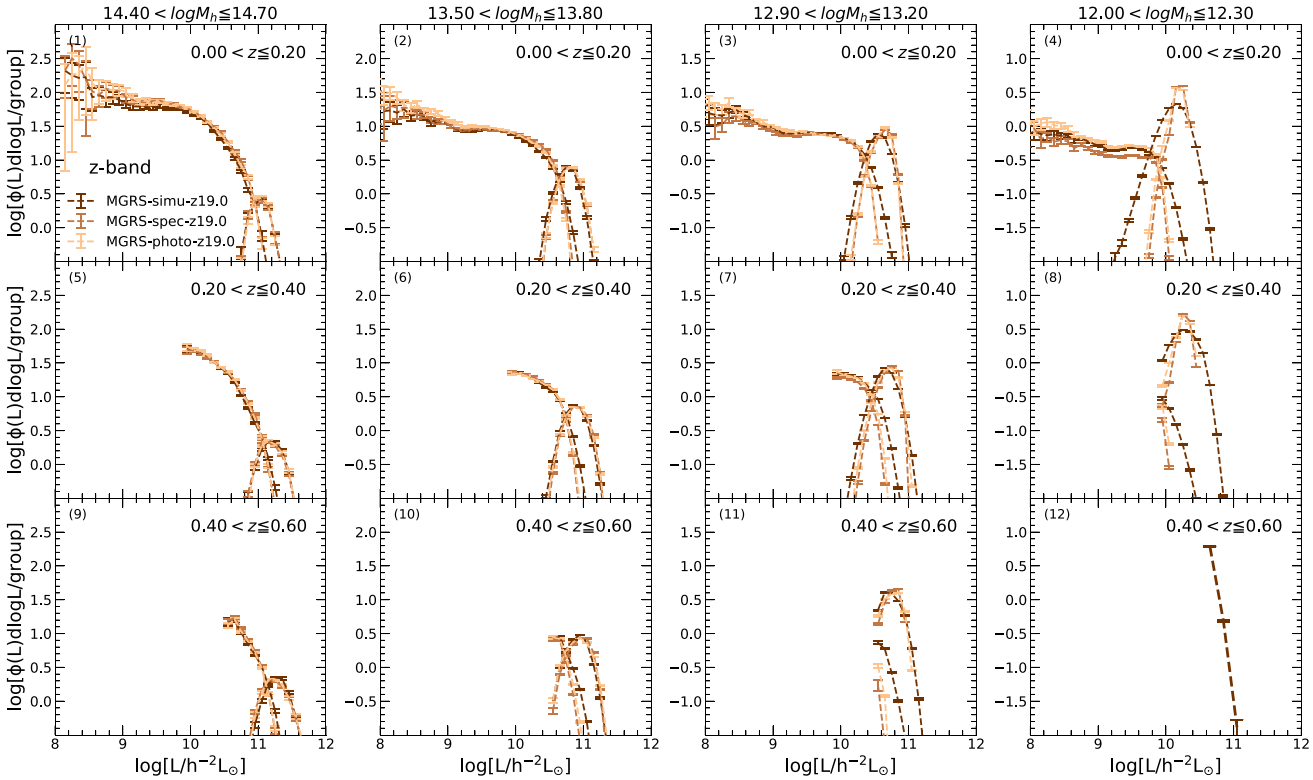

Figure 4. CLFs (z band) obtained from the MGRS. MGRS-simu, MGRS-spec, and MGRS-photo represent the true CLFs, those obtained from mock groups with spectroscopic, spectroscopic, and mixed spectroscopic and photometric redshifts, respectively. Each column corresponds to a different halo mass bin, and each row stands for a different redshift bin. The errors are obtained from the standard deviation of 200 bootstrap resamplings.

of approximately 0.05 dex. These comparisons demonstrate that the satellite CLFs of either a pure spec-z sample or a mixed sample (half photo-z and half spec-z) can also be well recovered, at least for satellite galaxies with $L \geqslant 10^8\, h^{-2}\, L_\odot$. The group finder will not induce significant bias in the CLF measurements in the DESI observations.

5. CLFs and CSMFs

With all of the above preparations, we set out to measure the CLFs and CSMFs from the DESI galaxy observational samples.

5.1. Global Properties

Before we move forward, we will present two sets of measurements of the global characteristics of groups that are essential components of the CLF and HOD theoretical framework: (1) the luminosity (or stellar mass) of the central galaxy–halo mass relation and (2) the satellite fraction, $f_{\rm sat}$.

The central galaxy luminosity (or stellar mass)–halo mass relation is a key factor in understanding how galaxies form and evolve in dark matter halos. We show in Figure 5 the central galaxy–halo mass ratios obtained from the LS DR9 group catalogs within $0 \leqslant z \leqslant 0.6$ for r-band luminosity, z-band luminosity, and stellar mass in the left, middle, and right panels, respectively. The magenta shaded region represents the Y1-BGS subsample, and the blue squares with error bars correspond to the SV3-BGS subsample. There is no significant difference between the spec-z subsample (SV3-BGS) and the half spec-z subsample (Y1-BGS). This is in agreement with the results of Section 4, which suggest that the photo-z error has a negligible effect on the CLFs. Generally, the luminosity (stellar mass) of the centrals has the largest luminosity (stellar mass) to halo mass ratio in halos with mass $\sim 10^{12}\, h^{-1}\, M_\odot$, then drops at the ends of low mass and high mass. This is consistent with previous findings, which are also shown in the right panel for comparison (Behroozi et al. 2013; Reddick et al. 2013; Moster et al. 2018), and is probably due to a combination of AGN feedback at the massive end and supernova feedback at the low-mass end (Yang et al. 2008).

In the HOD framework, the satellite fraction $f_{\rm sat}$ is considered one of the most important quantities in modeling the galaxy correlation functions. $f_{\rm sat}$ is defined as the ratio between the number of satellites and the number of all galaxies at fixed galaxy luminosity or the stellar mass bin. Since each halo only contains one central galaxy, the large-scale clustering of galaxies at fixed luminosity is significantly impacted by the fraction of the satellite galaxies.

The $f_{\rm sat}$ functions obtained from the SV3-BGS and Y1-BGS subsamples are displayed in Figure 6 for the redshift range $0 \leqslant z \leqslant 0.6$. The fraction of satellites is calculated by dividing the number of satellites by the total number of galaxies in a given luminosity or stellar mass bin normalized by the $V_{\rm max}$ factor. The error bars represent 3σ confidence levels obtained from 200 bootstrap resamplings. For accuracy, only results from luminosity bins with at least 600 galaxies are shown, which leads to a truncation of the SV3-BGS subsample at the faint end. The satellite fraction increases from close to 10% at the faint end to a maximum of around 30% at $L \sim 10^{9.5}\, h^{-2}\, L_\odot$ and then decreases to zero for the most luminous or massive galaxies. This 10% level of the satellite fraction in the faint end (low mass) is in agreement with the satellite-to-all subhalo

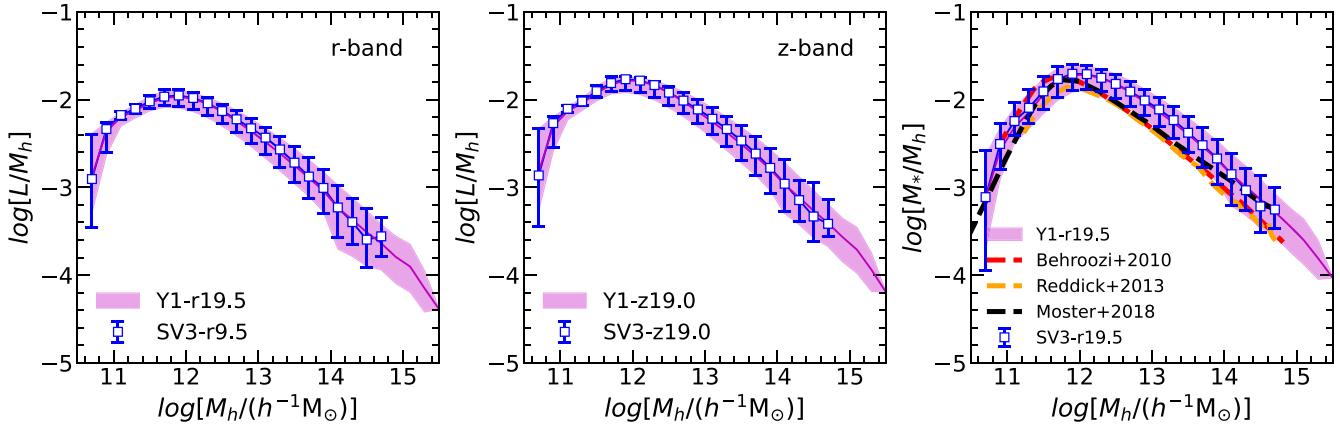

Figure 5. Central galaxy luminosity (stellar mass) vs. halo mass relations. The magenta shaded regions are results obtained from the Y1-BGS subsample. Blue squares with error bars are obtained from the SV3-BGS subsample. The shaded regions and error bars represent 1σ (68%) of scatters. Results from previous studies (Behroozi et al. 2013; Reddick et al. 2013; Moster et al. 2018) are also shown in the right panel for comparison.

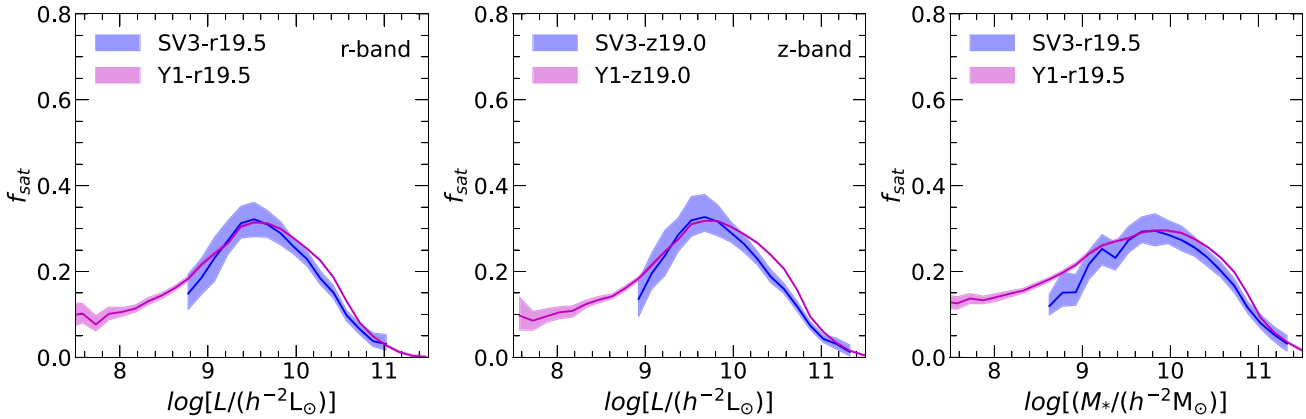

Figure 6. Fraction of satellite galaxies for Y1-BGS and SV3-BGS subsamples as a function of luminosity (left and middle panels for r band and z band, respectively) and stellar mass (right panel) using the $V_{\rm max}$ method. The error bars represent 3σ (99.8%) of the scatters. Note that for each luminosity bin, we removed data points whose total galaxy numbers are less than 600.

fraction at the low-mass end in our Jiutian simulations. However, it should be noted that this fraction might vary on the basis of simulation resolution, the techniques used for subhalo identification, and whether disrupted subhalos are included. From an observational standpoint, our group finder only detects the brightest group galaxies (BGGs). Skibba et al. (2011) noted that a specific fraction of central galaxies are not BGGs. Consequently, the satellite fraction estimated by our group finder can be somewhat underestimated. The results in the three panels demonstrate that $f_{\rm sat}$ is independent of the choice of galaxy stellar mass and luminosity, as well as the bands of luminosity.

5.2. CLFs Measured from DESI Observations

In this subsection, we directly measure the CLFs from the DESI observational data in multiple halo mass bins. As tested in Section 4, the CLFs can be reliably measured from both the spectroscopic and combined redshift data. However, the available spectroscopic sample in this study, SV3-BGS, only covers about 133 deg^2. Therefore, it can only provide CLF measurements for relatively bright galaxies. The Y1-BGS subsample, on the other hand, covers a much larger area of the sky and has a spectroscopic redshift completeness of ∼50%. According to Section 4.2, we have demonstrated that the mixed sample, with the same spectral completeness as Y1-BGS, can also provide a reliable CLF for luminosities $L \geqslant 10^8\,h^{-2}\,L_{\odot}$. We present the direct CLF results of the SV3-BGS and Y1-BGS subsamples. Here, a small correction factor obtained from Section 3.1 is applied to the Y1-BGS subsample. As we focus on relatively bright luminosity ranges ($L \gtrsim 10^8\,h^{-2}\,L_{\odot}$), even without such a correction, the general trends will remain almost unchanged.

Figure 7 shows the CLFs measured from the r band in different mass and redshift bins. Compared with those in Section 4.2, we find that the CLFs of DESI show a similar behavior to those obtained from the MGRS, in that Y1-BGS and SV3-BGS show very similar results. On the other hand, due to the much larger sky coverage of Y1-BGS, its CLFs in general show much better statistics and smaller error bars.

For comparison, we also show the r-band CLFs measured from SDSS observations in Yang et al. (2008) with black circles in the top panels of Figure 7. In this instance, we present results only for the three lower halo mass bins since their most massive bin covers a broader range of halo masses than ours.

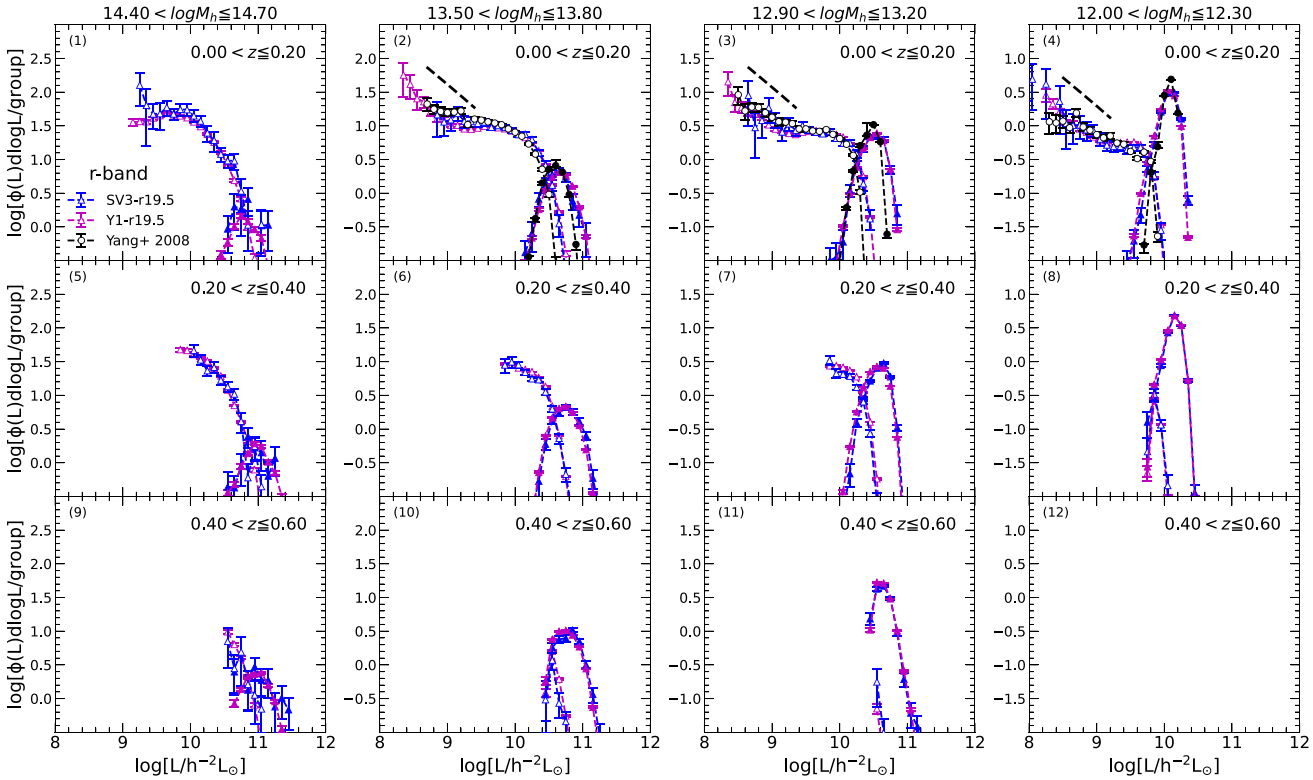

Figure 7. CLFs (r band) obtained from Y1-r19.5 (magenta triangles) and SV3-r19.5 (blue triangles) subsamples. Each column corresponds to a different halo mass bin, and each row stands for a different redshift bin. The error bars are obtained from the standard deviation of 200 bootstrap resamplings. We removed data points whose galaxy numbers are less than 10 in each luminosity bin of the Y1-BGS subsample. The short black dashed lines in the upper panels illustrate the slope of the subhalo mass function. Results from Yang et al. (2008) are also shown in the lowest redshift bin for comparison.

Generally, our findings are consistent with Yang et al. (2008). However, thanks to the DESI deeper imaging and spectroscopic surveys, our CLF measurements are able to reach the much fainter end and show a clear upturn. Quite interestingly, this kind of enhancement in the faint-end CLFs and CSMFs was already reported in previous works (e.g., Rodríguez-Puebla et al. 2013; Lan et al. 2016; Meng et al. 2023) using SDSS groups. By combing SDSS imaging data and SDSS group catalogs, Lan et al. (2016) found that the satellite CLFs of SDSS groups at redshift $0.01 \sim 0.05$ display a steep upturn at $L \lesssim 10^9\,h^{-2}\,L_\odot$ for all halo masses, mainly contributed by red galaxies.

Here, thanks to the much deeper DESI observations, we are able to obtain more reliable CLF measurements. Interestingly, we found that the slope of the upturn at $L \lesssim 10^9\,h^{-2}\,L_\odot$ is rather steep ($\alpha \sim -1 \pm 0.3$). The faint-end slope of the CLFs is in general agreement with that of the subhalo mass function, which is indicated by the black dashed line in the top panels, except for the most massive bin. This suggests that galaxies may have a roughly constant star formation efficiency in low-mass subhalos. According to Figure 5, a galaxy with a characteristic luminosity of $L \sim 10^9\,h^{-2}\,L_\odot$ lives in a halo with mass $M_h \sim 10^{11}\,h^{-1}\,M_\odot$. Halos with mass lower than this critical mass tend to form stars with a roughly constant efficiency.

Figure 8 shows the CLFs measured from the z band in different mass and redshift bins. Overall, the CLFs from the z band show similar trends as the r band, except that the ones in the z band are slightly shifted to the brighter end.

5.3. CSMFs Measured from DESI Observations

The CSMF, $\Phi(M_*M_h)$, is a key element in modeling the evolution of galaxies. It describes the average number of galaxies as a function of galaxy stellar mass M_* in a dark matter halo of a particular mass M_h. It is simpler and more common to use CSMF than CLF to access galaxy formation models because of the difficulty in converting mass to luminosity. When evaluating the CSMF, the completeness of the galaxy sample in terms of stellar mass shall also be properly taken into account. For each galaxy, we count the number of groups within the maximum redshift $z_{\rm max}$ and redshift range to calculate the CSMFs. The CSMFs obtained from the DESI observations are shown in Figure 9. The data points are taken from the SV3-BGS and Y1-BGS samples. The CSMFs have overall similarities with the CLF in terms of shape and features.

The above direct CLF/CSMF measurements that cover much larger redshift and luminosity/stellar mass ranges will be adopted in a subsequent study to understand the evolution of galaxies below redshift $z = 0.6$.

6. Discussion

In our measurements of the CLFs/CSMFs, we find a clear upturn at $L \lesssim 10^9\,h^{-2}\,L_\odot$. However, this trend is not clearly pronounced in the LFs/SMFs of SV3-BGS shown in Figure 2, which exhibit a slight drop below $L \lesssim 10^8\,h^{-2}\,L_\odot$. We set out to explore the clues for the potential discrepancy and find that the local void (LV) in our Universe is a possible reason (Chen et al. 2019).

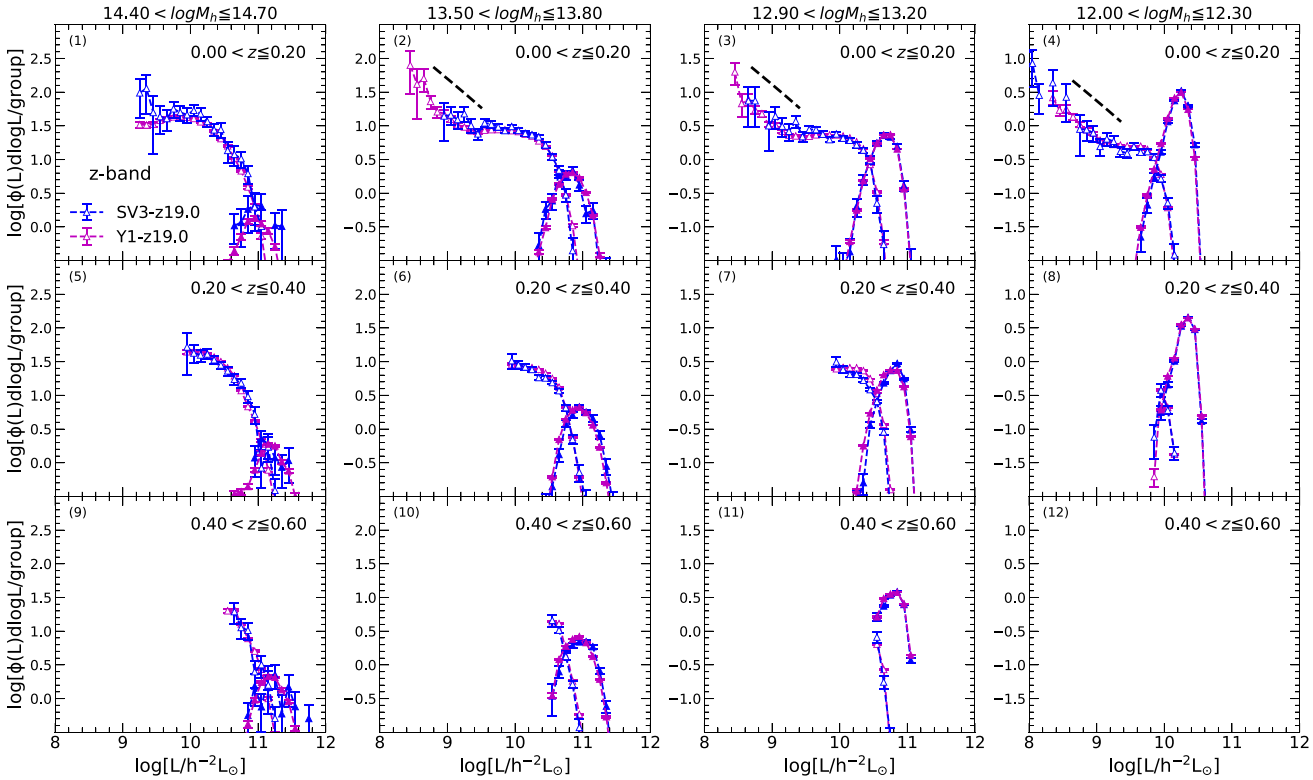

Figure 8. CLFs (z band) obtained from Y1-z19.0 (magenta triangles) and SV3-z19.0 (blue triangles) subsamples. Similarly to CLFs (r band), each column corresponds to a different halo mass bin, and each row stands for a different redshift bin. The error bars are obtained from the standard deviation of 200 bootstrap resamplings. We removed data points whose galaxy numbers are less than 10 in each luminosity bin of the Y1-BGS subsample. The short black dashed lines in the upper panels illustrate the slope of the subhalo mass function.

Table 4

Values of the Galaxy LFs and SMFs Obtained from the Y1-r19.5 Subsample after Being Modified by Correction Factors f_1 and f_2, Corresponding to Figure 10

L or M_* $[h^{-2}\ L_\odot]$ $[h^{-2}\ M_\odot]$	log $\Phi(L)$ − r band $[h^3\ \mathrm{Mpc}^{-3}\ d\ \log\ L]$			log $\Phi(M_*)$ $[h^3\ \mathrm{Mpc}^{-3}\ d\ \log\ M_*]$		
	Y1	Y1 + f_1	Y1 + f_1 + f_2	Y1	Y1 + f_1	Y1 + f_1 + f_2
6.05	$-0.8244^{+0.0988}_{-0.1281}$	$0.06482^{+0.0988}_{-0.1282}$	...	$-1.0045^{+0.0742}_{-0.0895}$	$-0.3407^{+0.0742}_{-0.0895}$	...
6.15	$-0.9495^{+0.1006}_{-0.1312}$	$-0.1161^{+0.1006}_{-0.1312}$	...	$-1.1299^{+0.0683}_{-0.0811}$	$-0.5188^{+0.0683}_{-0.0811}$	...
6.25	$-0.8858^{+0.0798}_{-0.0979}$	$-0.1061^{+0.0798}_{-0.0979}$	...	$-0.8738^{+0.0691}_{-0.0822}$	$-0.3129^{+0.0691}_{-0.0822}$	...
6.35	$-0.7447^{+0.0539}_{-0.0616}$	$-0.0168^{+0.0539}_{-0.0616}$	...	$-0.9529^{+0.0697}_{-0.0831}$	$-0.4397^{+0.0697}_{-0.0831}$	...
6.45	$-0.8351^{+0.0594}_{-0.0689}$	$-0.1568^{+0.0594}_{-0.0689}$	...	$-1.0227^{+0.0656}_{-0.0773}$	$-0.5547^{+0.0656}_{-0.0773}$	...
6.55	$-0.8046^{+0.0495}_{-0.0559}$	$-0.1739^{+0.0495}_{-0.0559}$	...	$-0.9623^{+0.0447}_{-0.0498}$	$-0.5371^{+0.0447}_{-0.0498}$	...
6.65	$-0.9882^{+0.0521}_{-0.0593}$	$-0.4030^{+0.0521}_{-0.0593}$	...	$-1.1043^{+0.0404}_{-0.0446}$	$-0.7195^{+0.0404}_{-0.0446}$	...
6.75	$-1.0307^{+0.0369}_{-0.0404}$	$-0.4890^{+0.0369}_{-0.0404}$	...	$-1.1221^{+0.0416}_{-0.0460}$	$-0.7751^{+0.0416}_{-0.0460}$	...
6.85	$-1.0179^{+0.0372}_{-0.0407}$	$-0.5176^{+0.0372}_{-0.0407}$	...	$-1.2026^{+0.0287}_{-0.0307}$	$-0.8911^{+0.0287}_{-0.0307}$	...
6.95	$-1.0794^{+0.0335}_{-0.0364}$	$-0.6185^{+0.0335}_{-0.0364}$	...	$-1.2648^{+0.0286}_{-0.0307}$	$-0.9863^{+0.0286}_{-0.0307}$	...
7.05	$-1.1274^{+0.0287}_{-0.0307}$	$-0.7038^{+0.0287}_{-0.0307}$	...	$-1.3167^{+0.0259}_{-0.0276}$	$-1.0687^{+0.0259}_{-0.0276}$	...
7.15	$-1.2113^{+0.0307}_{-0.0330}$	$-0.8229^{+0.0307}_{-0.0330}$	...	$-1.3448^{+0.0213}_{-0.0224}$	$-1.1248^{+0.0213}_{-0.0224}$	...
7.25	$-1.2318^{+0.0247}_{-0.0262}$	$-0.8766^{+0.0247}_{-0.0262}$	...	$-1.3473^{+0.0178}_{-0.0186}$	$-1.1528^{+0.0178}_{-0.0186}$	...
7.35	$-1.2753^{+0.0215}_{-0.0226}$	$-0.9512^{+0.0215}_{-0.0226}$	$-0.2555^{+0.0215}_{-0.0226}$	$-1.3313^{+0.0163}_{-0.0169}$	$-1.1600^{+0.0163}_{-0.0169}$	$-0.4644^{+0.0163}_{-0.0169}$
7.45	$-1.3208^{+0.0180}_{-0.0187}$	$-1.0258^{+0.0180}_{-0.0187}$	$-0.3301^{+0.0180}_{-0.0187}$	$-1.3178^{+0.0122}_{-0.0125}$	$-1.1671^{+0.0122}_{-0.0125}$	$-0.4715^{+0.0122}_{-0.0125}$
7.55	$-1.2930^{+0.0159}_{-0.0165}$	$-1.0250^{+0.0159}_{-0.0165}$	$-0.4627^{+0.0159}_{-0.0165}$	$-1.3325^{+0.0108}_{-0.0110}$	$-1.2000^{+0.0108}_{-0.0110}$	$-0.6377^{+0.0108}_{-0.0110}$
7.65	$-1.2980^{+0.0116}_{-0.0119}$	$-1.055^{+0.0116}_{-0.0119}$	$-0.6023^{+0.0116}_{-0.0119}$	$-1.3320^{+0.0088}_{-0.0090}$	$-1.2152^{+0.0088}_{-0.0090}$	$-0.7626^{+0.0088}_{-0.0090}$
7.75	$-1.3157^{+0.0122}_{-0.0125}$	$-1.0955^{+0.0122}_{-0.0125}$	$-0.7102^{+0.0122}_{-0.0125}$	$-1.3237^{+0.0077}_{-0.0079}$	$-1.2202^{+0.0077}_{-0.0079}$	$-0.8349^{+0.0077}_{-0.0079}$
7.85	$-1.2772^{+0.0090}_{-0.0092}$	$-1.0779^{+0.0090}_{-0.0092}$	$-0.7678^{+0.0090}_{-0.0092}$	$-1.3311^{+0.0064}_{-0.0065}$	$-1.2385^{+0.0064}_{-0.0065}$	$-0.9284^{+0.0064}_{-0.0065}$
7.95	$-1.2571^{+0.0072}_{-0.0073}$	$-1.0765^{+0.0072}_{-0.0073}$	$-0.8485^{+0.0072}_{-0.0073}$	$-1.3357^{+0.0060}_{-0.0060}$	$-1.2515^{+0.0060}_{-0.0060}$	$-1.0234^{+0.0060}_{-0.0060}$
8.05	$-1.2581^{+0.0064}_{-0.0065}$	$-1.0941^{+0.0064}_{-0.0065}$	$-0.9394^{+0.0064}_{-0.0065}$	$-1.3403^{+0.0049}_{-0.0050}$	$-1.2619^{+0.0049}_{-0.0050}$	$-1.1071^{+0.0049}_{-0.0050}$
8.15	$-1.2655^{+0.0050}_{-0.0051}$	$-1.1162^{+0.0050}_{-0.0051}$	$-1.0238^{+0.0050}_{-0.0051}$	$-1.3625^{+0.0055}_{-0.0055}$	$-1.2876^{+0.0055}_{-0.0055}$	$-1.1952^{+0.0055}_{-0.0055}$
8.25	$-1.2686^{+0.0048}_{-0.0048}$	$-1.132^{+0.0048}_{-0.0048}$	$-1.0961^{+0.0048}_{-0.0048}$	$-1.3818^{+0.0039}_{-0.0039}$	$-1.3079^{+0.0039}_{-0.0039}$	$-1.2720^{+0.0039}_{-0.0039}$
8.35	$-1.2770^{+0.0041}_{-0.0041}$	$-1.1509^{+0.0041}_{-0.0041}$	$-1.1521^{+0.0041}_{-0.0041}$	$-1.4013^{+0.0040}_{-0.0040}$	$-1.3259^{+0.0040}_{-0.0040}$	$-1.3272^{+0.0040}_{-0.0040}$

Table 4
(Continued)

L or M_* $[h^{-2}\ L_\odot]$ $[h^{-2}\ M_\odot]$	log $\Phi(L)$ − r band $[h^3\ \mathrm{Mpc}^{-3}\ d\ \log\ L]$			log $\Phi(M_*)$ $[h^3\ \mathrm{Mpc}^{-3}\ d\ \log\ M_*]$		
	Y1	Y1 + f_1	Y1 + f_1 + f_2	Y1	Y1 + f_1	Y1 + f_1 + f_2
8.45	$-1.2924^{+0.0036}_{-0.0037}$	$-1.2924^{+0.0036}_{-0.0037}$	$-1.2937^{+0.0036}_{-0.0037}$	$-1.4228^{+0.0036}_{-0.0037}$	$-1.4228^{+0.0036}_{-0.0037}$	$-1.4241^{+0.0036}_{-0.0037}$
8.55	$-1.3251^{+0.0030}_{-0.0030}$	$-1.3251^{+0.0030}_{-0.0030}$	$-1.3251^{+0.0030}_{-0.0030}$	$-1.4642^{+0.0671}_{-0.0794}$	$-1.4642^{+0.0671}_{-0.0794}$	$-1.4642^{+0.0671}_{-0.0794}$
8.65	$-1.3700^{+0.0022}_{-0.0022}$	$-1.3700^{+0.0022}_{-0.0022}$	$-1.3700^{+0.0022}_{-0.0022}$	$-1.4986^{+0.0028}_{-0.0029}$	$-1.4986^{+0.0028}_{-0.0029}$	$-1.4986^{+0.0028}_{-0.0029}$
8.75	$-1.4067^{+0.0022}_{-0.0022}$	$-1.4067^{+0.0022}_{-0.0022}$	$-1.4067^{+0.0022}_{-0.0022}$	$-1.5257^{+0.0026}_{-0.0027}$	$-1.5257^{+0.0026}_{-0.0027}$	$-1.5257^{+0.0026}_{-0.0027}$
8.85	$-1.4502^{+0.0019}_{-0.0019}$	$-1.4502^{+0.0019}_{-0.0019}$	$-1.4502^{+0.0019}_{-0.0019}$	$-1.5697^{+0.0020}_{-0.0020}$	$-1.5697^{+0.0020}_{-0.0020}$	$-1.5697^{+0.0020}_{-0.0020}$
8.95	$-1.4815^{+0.0019}_{-0.0019}$	$-1.4815^{+0.0019}_{-0.0019}$	$-1.4815^{+0.0019}_{-0.0019}$	$-1.6000^{+0.0019}_{-0.0019}$	$-1.6000^{+0.0019}_{-0.0019}$	$-1.6000^{+0.0019}_{-0.0019}$
9.05	$-1.5181^{+0.0017}_{-0.0017}$	$-1.5181^{+0.0017}_{-0.0017}$	$-1.5181^{+0.0017}_{-0.0017}$	$-1.6228^{+0.0020}_{-0.0020}$	$-1.6228^{+0.0020}_{-0.0020}$	$-1.6228^{+0.0020}_{-0.0020}$
9.15	$-1.5494^{+0.0015}_{-0.0015}$	$-1.5494^{+0.0015}_{-0.0015}$	$-1.5494^{+0.0015}_{-0.0015}$	$-1.6316^{+0.0016}_{-0.0016}$	$-1.6316^{+0.0016}_{-0.0016}$	$-1.6316^{+0.0016}_{-0.0016}$
9.25	$-1.5641^{+0.0012}_{-0.0012}$	$-1.5641^{+0.0012}_{-0.0012}$	$-1.5641^{+0.0012}_{-0.0012}$	$-1.6516^{+0.0016}_{-0.0016}$	$-1.6516^{+0.0016}_{-0.0016}$	$-1.6516^{+0.0016}_{-0.0016}$
9.35	$-1.5750^{+0.0012}_{-0.0013}$	$-1.5750^{+0.0012}_{-0.0013}$	$-1.5750^{+0.0012}_{-0.0013}$	$-1.6771^{+0.0023}_{-0.0023}$	$-1.6771^{+0.0023}_{-0.0023}$	$-1.6771^{+0.0023}_{-0.0023}$
9.45	$-1.5771^{+0.0009}_{-0.0009}$	$-1.5771^{+0.0009}_{-0.0009}$	$-1.5771^{+0.0009}_{-0.0009}$	$-1.7021^{+0.0012}_{-0.0012}$	$-1.7021^{+0.0012}_{-0.0012}$	$-1.7021^{+0.0012}_{-0.0012}$
9.55	$-1.5974^{+0.0008}_{-0.0008}$	$-1.5974^{+0.0008}_{-0.0008}$	$-1.5974^{+0.0008}_{-0.0008}$	$-1.7217^{+0.0011}_{-0.0011}$	$-1.7217^{+0.0011}_{-0.0011}$	$-1.7217^{+0.0011}_{-0.0011}$
9.65	$-1.6253^{+0.0008}_{-0.0008}$	$-1.6253^{+0.0008}_{-0.0008}$	$-1.6253^{+0.0008}_{-0.0008}$	$-1.7293^{+0.0009}_{-0.0009}$	$-1.7293^{+0.0009}_{-0.0009}$	$-1.7293^{+0.0009}_{-0.0009}$
9.75	$-1.6601^{+0.0006}_{-0.0006}$	$-1.6601^{+0.0006}_{-0.0006}$	$-1.6601^{+0.0006}_{-0.0006}$	$-1.7453^{+0.0008}_{-0.0008}$	$-1.7453^{+0.0008}_{-0.0008}$	$-1.7453^{+0.0008}_{-0.0008}$
9.85	$-1.7123^{+0.0007}_{-0.0007}$	$-1.7123^{+0.0007}_{-0.0007}$	$-1.7123^{+0.0007}_{-0.0007}$	$-1.7616^{+0.0008}_{-0.0008}$	$-1.7616^{+0.0008}_{-0.0008}$	$-1.7616^{+0.0008}_{-0.0008}$
9.95	$-1.7757^{+0.0007}_{-0.0007}$	$-1.7757^{+0.0007}_{-0.0007}$	$-1.7757^{+0.0007}_{-0.0007}$	$-1.7861^{+0.0008}_{-0.0008}$	$-1.7861^{+0.0008}_{-0.0008}$	$-1.7861^{+0.0008}_{-0.0008}$
10.05	$-1.8442^{+0.0007}_{-0.0007}$	$-1.8442^{+0.0007}_{-0.0007}$	$-1.8442^{+0.0007}_{-0.0007}$	$-1.8118^{+0.0007}_{-0.0007}$	$-1.8118^{+0.0007}_{-0.0007}$	$-1.8118^{+0.0007}_{-0.0007}$
10.15	$-1.9324^{+0.0008}_{-0.0008}$	$-1.9324^{+0.0008}_{-0.0008}$	$-1.9324^{+0.0008}_{-0.0008}$	$-1.8482^{+0.0008}_{-0.0008}$	$-1.8482^{+0.0008}_{-0.0008}$	$-1.8482^{+0.0008}_{-0.0008}$
10.25	$-2.0419^{+0.0009}_{-0.0009}$	$-2.0419^{+0.0009}_{-0.0009}$	$-2.0419^{+0.0009}_{-0.0009}$	$-1.8975^{+0.0008}_{-0.0008}$	$-1.8975^{+0.0008}_{-0.0008}$	$-1.8975^{+0.0008}_{-0.0008}$
10.35	$-2.1730^{+0.0010}_{-0.0010}$	$-2.1730^{+0.0010}_{-0.0010}$	$-2.1730^{+0.0010}_{-0.0010}$	$-1.9553^{+0.0010}_{-0.0010}$	$-1.9553^{+0.0010}_{-0.0010}$	$-1.9553^{+0.0010}_{-0.0010}$
10.45	$-2.3346^{+0.0012}_{-0.0012}$	$-2.3346^{+0.0012}_{-0.0012}$	$-2.3346^{+0.0012}_{-0.0012}$	$-2.0434^{+0.0010}_{-0.0010}$	$-2.0434^{+0.0010}_{-0.0010}$	$-2.0434^{+0.0010}_{-0.0010}$
10.55	$-2.5286^{+0.0015}_{-0.0015}$	$-2.5286^{+0.0015}_{-0.0015}$	$-2.5286^{+0.0015}_{-0.0015}$	$-2.1502^{+0.0011}_{-0.0011}$	$-2.1502^{+0.0011}_{-0.0011}$	$-2.1502^{+0.0011}_{-0.0011}$
10.65	$-2.7615^{+0.0025}_{-0.0025}$	$-2.7615^{+0.0025}_{-0.0025}$	$-2.7615^{+0.0025}_{-0.0025}$	$-2.2771^{+0.0012}_{-0.0012}$	$-2.2771^{+0.0012}_{-0.0012}$	$-2.2771^{+0.0012}_{-0.0012}$
10.75	$-3.0362^{+0.0031}_{-0.0031}$	$-3.0362^{+0.0031}_{-0.0031}$	$-3.0362^{+0.0031}_{-0.0031}$	$-2.4380^{+0.0013}_{-0.0013}$	$-2.4380^{+0.0013}_{-0.0013}$	$-2.4380^{+0.0013}_{-0.0013}$
10.85	$-3.3658^{+0.0048}_{-0.0048}$	$-3.3658^{+0.0048}_{-0.0048}$	$-3.3658^{+0.0048}_{-0.0048}$	$-2.6302^{+0.0019}_{-0.0019}$	$-2.6302^{+0.0019}_{-0.0019}$	$-2.6302^{+0.0019}_{-0.0019}$
10.95	$-3.7564^{+0.0073}_{-0.0074}$	$-3.7564^{+0.0073}_{-0.0074}$	$-3.7564^{+0.0073}_{-0.0074}$	$-2.8699^{+0.0023}_{-0.0023}$	$-2.8699^{+0.0023}_{-0.0023}$	$-2.8699^{+0.0023}_{-0.0023}$
11.05	$-4.1972^{+0.0127}_{-0.0131}$	$-4.1972^{+0.0127}_{-0.0131}$	$-4.1972^{+0.0127}_{-0.0131}$	$-3.1467^{+0.0034}_{-0.0035}$	$-3.1467^{+0.0034}_{-0.0035}$	$-3.1467^{+0.0034}_{-0.0035}$
11.15	$-4.7686^{+0.0224}_{-0.0236}$	$-4.7686^{+0.0224}_{-0.0236}$	$-4.7686^{+0.0224}_{-0.0236}$	$-3.4861^{+0.0050}_{-0.0051}$	$-3.4861^{+0.0050}_{-0.0051}$	$-3.4861^{+0.0050}_{-0.0051}$
11.25	$-5.4712^{+0.0466}_{-0.0522}$	$-5.4712^{+0.0466}_{-0.0522}$	$-5.4712^{+0.0466}_{-0.0522}$	$-3.8765^{+0.0077}_{-0.0079}$	$-3.8765^{+0.0077}_{-0.0079}$	$-3.8765^{+0.0077}_{-0.0079}$
11.35	$-6.2598^{+0.1085}_{-0.1451}$	$-6.2598^{+0.1085}_{-0.1451}$	$-6.2598^{+0.1085}_{-0.1451}$	$-4.3476^{+0.0134}_{-0.0138}$	$-4.3476^{+0.0134}_{-0.0138}$	$-4.3476^{+0.0134}_{-0.0138}$
11.45	$-6.7732^{+0.1882}_{-0.3395}$	$-6.7732^{+0.1882}_{-0.3395}$	$-6.7732^{+0.1882}_{-0.3395}$	$-4.9537^{+0.0264}_{-0.0281}$	$-4.9537^{+0.0264}_{-0.0281}$	$-4.9537^{+0.0264}_{-0.0281}$
11.55	...	...	...	$-5.6075^{+0.0516}_{-0.0586}$	$-5.6075^{+0.0516}_{-0.0586}$	$-5.6075^{+0.0516}_{-0.0586}$
11.65	...	...	...	$-6.5013^{+0.1361}_{-0.1993}$	$-6.5013^{+0.1361}_{-0.1993}$	$-6.5013^{+0.1361}_{-0.1993}$
11.75	...	...	...	$-7.0417^{+0.2285}_{-0.5120}$	$-7.0417^{+0.2285}_{-0.5120}$	$-7.0417^{+0.2285}_{-0.5120}$

Note. The error bars of the corrected values inherit the original ones.

The Milky Way resides within an LV in the Universe. To mitigate the influence of this LV on the LF and SMF measurements, Chen et al. (2019) introduced a comprehensive correction approach using the ELUCID simulation (e.g., Wang et al. 2014, 2016; Yang et al. 2018) by comparing the LFs/SMFs from the SDSS region to those across the entire simulation box. Without this correction, the faint end of the galaxy LFs derived from SDSS would be notably diminished.

To assess the constraining power of Y1-BGS in LFs at $L \gtrsim 10^{8.2}\ h^{-1}\ L_\odot$, we compare our measurements of Y1-BGS that incorporate the photo-z correction factor f_1 from Section 3 with those obtained from SDSS by Chen et al. (2019) in Figure 10. The galaxies in the two observations are both k-corrected to $z = 0.1$, and the primary difference between these two samples is their redshift range, as $0 < z < 0.2$ in Y1-BGS and $0 < z < 0.12$ in Chen et al. (2019). We find that the LF results measured directly by Y1-BGS with the photo-z correction factor f_1 are in good agreement with those obtained from SDSS after LV correction. Y1-BGS, which has observed wide sky regions and is much deeper, should suffer from the LV effect in the much fainter luminosity ranges. The good agreement demonstrates that the LV correction factor obtained by Chen et al. (2019) in the range of $10^{8.2}\ h^{-2}\ L_\odot$ to $10^9\ h^{-2}\ L_\odot$ works remarkably well. Additionally, we compare our results using the correction factor f_1 with earlier studies (Loveday et al. 2015; Blanton et al. 2005; Baldry et al. 2012) as depicted in Figure 10, finding that the trends in the LFs and SMFs generally align.

Considering that the apparent magnitude limit of Y1-r19.5 is nearly 2 mag fainter than that of Chen et al. (2019), which is 17.6, the impact of the LV on the LFs might also appear in the 2 mag fainter ranges, that is, below $L \lesssim 10^{8.2}\ h^{-1}\ L_\odot$. In this section, we apply the same correction factor obtained by Chen et al. (2019) to our LF and SMF measurements at $L \lesssim 10^{8.2}\ h^{-1}\ L_\odot$, shifted to the fainter end by 0.8 dex in terms of luminosity or stellar mass. Our LF and SMF results with photo-z correction factor f_1 are shown in Figure 10, illustrated by blue dots with error bars. The results with the additional cosmic

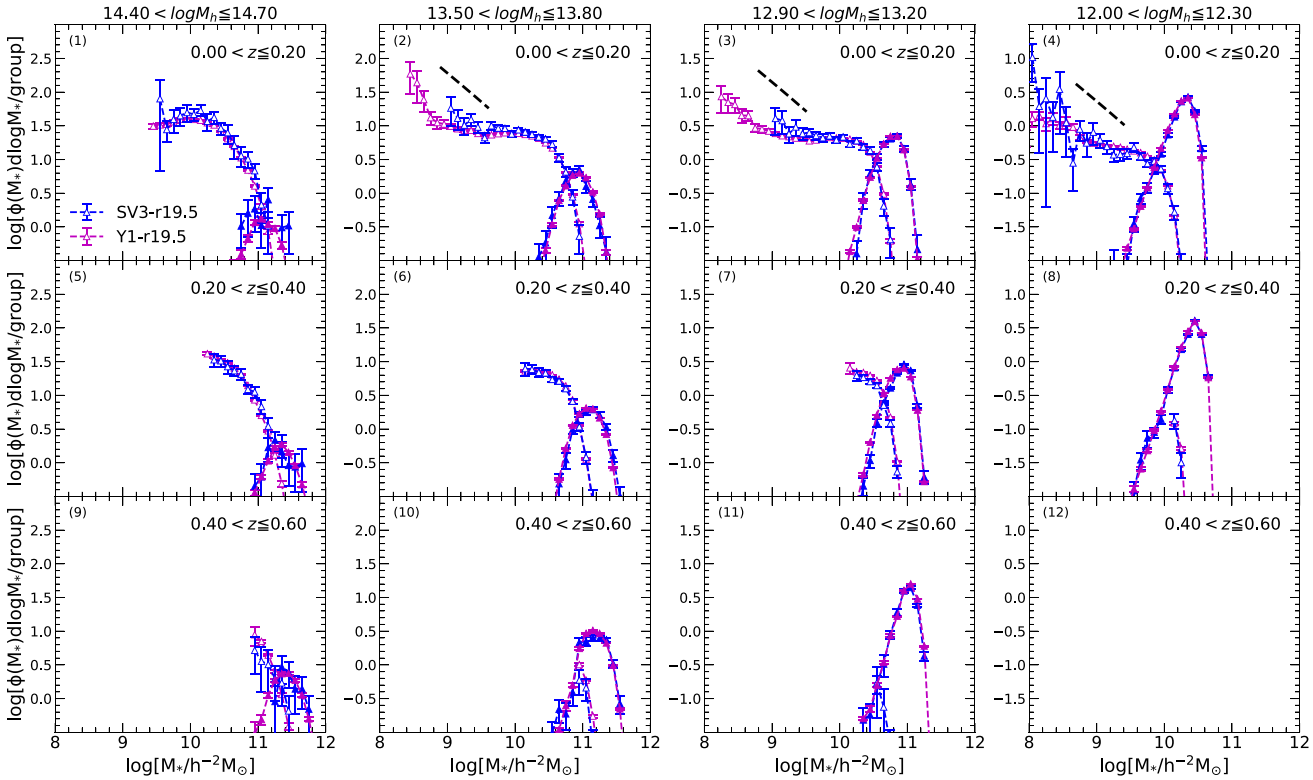

Figure 9. CSMFs obtained from the combination of Y1-r19.5 (magenta triangles) and SV3-r19.5 (blue triangles) subsamples. Similarly to the CLFs above, each column corresponds to a different halo mass bin, and each row stands for a different redshift bin. The error bars are obtained from the standard deviation of 200 bootstrap resamplings. We removed data points whose galaxy numbers are less than 10 in each stellar mass bin of the Y1-BGS subsample. The short black dashed lines in the upper panels illustrate the slope of the subhalo mass function.

variance correction factor f_2 are shown by blue stars. It is evident that there is a considerable difference in the faint-end slope, with $\Delta\alpha \sim 0.5$ comparing the slope in the range of $10^{7.4}\ h^{-2}\ L_\odot \sim 10^{8.5}\ h^{-2}\ L_\odot$ with that of $L \gtrsim 10^{8.5}\ h^{-2}\ L_\odot$.

As a reference, we show in each panel of Figure 10 the low-mass end slope of the halo mass function using a short black dashed line. Upon closer inspection, it is notable that the slopes of the LF and SMF match the typical halo mass function at the very faint end. This behavior is now in good agreement with our CLF measurements, in that for both total and satellite galaxies with luminosity/stellar mass less than $\sim 10^9\ h^{-2}\ L_\odot$ (or $h^{-2}\ M_\odot$), they show roughly consistent galaxy–halo connections. In addition, it suggests that galaxy formation in low-mass halos could still be quite efficient, regardless of halo mass. This would be contrary to the standard theories of galaxy formation, which usually invoke stellar winds, supernova feedback, etc., to reduce star formation efficiency toward the low-mass end.

It should be noted that our analysis did not incorporate surface brightness corrections for lower-mass objects. Blanton et al. (2005) comprehensively discussed the issue of missing low-surface-brightness galaxies due to the SDSS pipeline. Nevertheless, with the deeper imaging capabilities and enhancements in the DESI LS pipeline, we anticipate that this problem will be less significant compared to SDSS. According to Figure 2 in Zou et al. (2019), which illustrates the detection completeness of sources in the DESI LS compared to the COSMOS space observation, our BGS galaxies achieve a completeness of more than 97%.

7. Summary

In this paper, we leverage the two recent DESI observational subsamples, SV3-BGS and Y1-BGS, to update the seed catalog of LS DR9 for our group finder. The SV3-BGS, despite the limited coverage of 133 $\deg^2$, contains the most complete spectroscopic redshift data. In contrast, the Y1-BGS, with only half of the spectroscopic redshift completeness, achieves a sky coverage that is 90 times larger than SV3-BGS. We obtain a galaxy group catalog by applying the extended version of halo-based group finder (Yang et al. 2021) to this updated seed catalog. Based on the assessments using MGRS spec-z and photo-z mock galaxy samples constructed based on Jiutian simulation, we investigated the galaxy LFs, SMFs, CLFs, and CSMFs in three redshift bins up to $z = 0.6$. Our main results can be summarized as follows.

1. We measure the galaxy LFs and SMFs in three different redshift bins. We find that utilization of photometric redshift in the mixed subsample will somewhat suppress the LFs and SMFs at the very faint/low-mass end in the lowest redshift bin.
2. We constructed an MGRS galaxy catalog based on Jiutian simulation using the LFs of Y1-BGS by applying the photo-z correction factor. To mimic the redshift completeness of the SV3-BGS and Y1-BGS subsamples, we have constructed two sets of redshifts, MGRS-spec and MGRS-photo. By applying the same group finder to the two sets of MGRSs, we use the resulting group catalogs to evaluate the reliability of the CLF

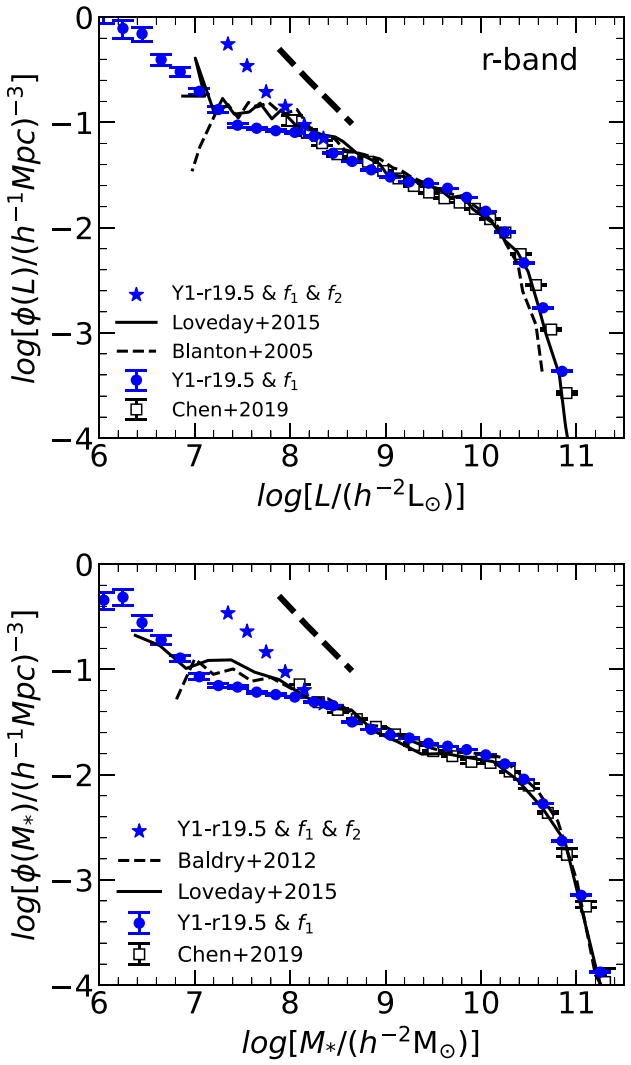

Figure 10. LFs and SMFs of the Y1-r19.5 subsample and those obtained by Chen et al. (2019) based on SDSS DR7. The blue symbols correspond to redshift ranges [0.00, 0.20], and the black open squares and corresponding error bars are from Chen et al. (2019): [0.01, 0.12]. f_1 stand for the photo-z correction factor, and f_2 is the cosmic variance correction factor. Values of data points are listed in Table 4. The short black dashed line illustrates the slope of the low-mass end of the halo mass function. Results from previous studies (Loveday et al. 2015; Blanton et al. 2005; Baldry et al. 2012) are also shown for comparison.

measurements. Compared to the true values, the two MGRS samples demonstrate that the central galaxy CLFs can be accurately recovered using both spec-z and photo-z in all redshift and halo mass bins, except for the lowest halo mass bin. The CLFs of the satellite galaxies are slightly underestimated by approximately 0.05 dex using spec-z.

3. We derived the central luminosity (or stellar mass)–host halo mass relations and the satellite fraction based on the galaxy group catalogs constructed from the SV3-BGS and Y1-BGS observational subsamples, which extend down to a luminosity or stellar mass of $\sim 10^{7.5}\,h^{-2}\,L_\odot$ ($h^{-2}\,M_\odot$). We found that the satellite fraction peaks at $\sim 10^{9.5}\,h^{-2}\,L_\odot$ at about the 30% level and decreases to 10% at the low-luminosity (or stellar mass) end.
4. Based on the validation of the group finder on our CLF measurements, we provide our observational measurements of CLFs and CSMFs at $L > 10^8\,h^{-2}\,L_\odot$ ($h^{-2}\,M_\odot$) from the SV3-BGS and Y1-BGS subsamples in a wide halo mass range and three redshift bins. Our analysis reveals an upturn in the CLFs and CSMFs at the faint (or low stellar mass) end below $10^9\,h^{-2}\,L_\odot$ (or $h^{-2}\,M_\odot$). Remarkably, the slope of this upturn is in nice agreement with that of the subhalo mass functions.
5. After taking into account the photo-z correction factor f_1 and LV correction factor f_2, the LFs and SMFs we obtained from DESI observation may also reveal a continuous upturn below $10^9\,h^{-2}\,L_\odot$ (or $h^{-2}\,M_\odot$), similar to those in the CLFs and CSMFs. The slope is in nice agreement with that of the halo mass function at the low-mass end.

This study provides a comprehensive analysis of the LFs, SMFs, CLFs, and CSMFs of galaxies across a broad range of redshifts and halo mass bins, combining both observed and mock galaxy samples. These measurements also span large luminosity (or stellar mass) ranges of $\gtrsim 10^{6.5}\,h^{-2}\,L_\odot$ (or $h^{-2}\,M_\odot$) at low redshift $z \sim 0.1$ and $\gtrsim 10^{10.5}\,h^{-2}\,L_\odot$ (or $h^{-2}\,M_\odot$) at higher redshift $z \sim 0.5$. The intriguing upturn feature in the faint (low-mass) end of LFs/SMFs/CLFs/CSMFs carries significant implications for refining the CLF model. Moreover, it provides valuable insights into the formation and evolution mechanisms of galaxies in the very low-mass halo. We will perform related investigations in a subsequent work.

Acknowledgments

The authors thank Antonella Palmese and the anonymous referee for valuable comments that improved the presentation of this paper. This work is supported by the National Key R&D Program of China (2023YFA1607800, 2023YFA1607804), the National Science Foundation of China (Nos. 11833005, 11890692, 11621303, 12141302), "the Fundamental Research Funds for the Central Universities," 111 project No. B20019, and Shanghai Natural Science Foundation, grant No.19ZR1466800. We acknowledge the science research grants from the China Manned Space Project with Nos. CMS-CSST-2021-A02, CMS-CSST-2021-A03. The computations in this paper were run on the Gravity Supercomputer at Shanghai Jiao Tong University.

This research used data obtained with the Dark Energy Spectroscopic Instrument (DESI). DESI construction and operations is managed by the Lawrence Berkeley National Laboratory. This material is based upon work supported by the U.S. Department of Energy, Office of Science, Office of High-Energy Physics, under contract No. DEAC0205CH11231, and by the National Energy Research Scientific Computing Center, a DOE Office of Science User Facility under the same contract. Additional support for DESI was provided by the U.S. National Science Foundation (NSF), Division of Astronomical Sciences, under contract No. AST-0950945 to the NSF's National Optical-Infrared Astronomy Research Laboratory; the Science and Technology Facilities Council of the United Kingdom; the Gordon and Betty Moore Foundation; the Heising-Simons Foundation; the French Alternative Energies and Atomic Energy Commission (CEA); the National Council of Science and Technology of Mexico (CONACYT); the Ministry of Science and Innovation of Spain (MICINN), and the DESI Member Institutions: www.desi.lbl.gov/collaborating-institutions.

The DESI Legacy Imaging Surveys consist of three individual and complementary projects: the Dark Energy Camera Legacy Survey (DECaLS), the Beijing–Arizona Sky Survey (BASS), and the Mayall z-band Legacy Survey (MzLS). DECaLS, BASS, and MzLS together include data obtained, respectively, at the Blanco telescope, Cerro Tololo Inter-American Observatory, NSF's NOIRLab; the Bok telescope, Steward Observatory, University of Arizona; and the Mayall telescope, Kitt Peak National Observatory, NOIRLab. NOIRLab is operated by the Association of Universities for Research in Astronomy (AURA) under a cooperative agreement with the National Science Foundation. Pipeline processing and analyses of the data were supported by NOIRLab and the Lawrence Berkeley National Laboratory (LBNL). Legacy Imaging Surveys also uses data products from the Near-Earth Object Wide-field Infrared Survey Explorer (NEOWISE), a project of the Jet Propulsion Laboratory/California Institute of Technology, funded by the National Aeronautics and Space Administration. Legacy Imaging Surveys was supported by the Director, Office of Science, Office of High Energy Physics of the U.S. Department of Energy; the National Energy Research Scientific Computing Center, a DOE Office of Science User Facility; the U.S. National Science Foundation, Division of Astronomical Sciences; the National Astronomical Observatories of China; the Chinese Academy of Sciences; and the Chinese National Natural Science Foundation. LBNL is managed by the Regents of the University of California under contract to the U.S. Department of Energy. The complete acknowledgments can be found at https://www.legacysurvey.org/acknowledgment/.

We additionally made use of Astropy, a community-developed core Python package for Astronomy (Astropy Collaboration et al. 2018), IPython (Perez & Granger 2007), Matplotlib (Hunter 2007), and TOPCAT (Taylor 2005; http://www.starlink.ac.uk/topcat/).

Appendix A
Cosmic Variance in the SV3-BGS Subsample

When performing the LF measurements from the SV3-BGS subsamples using the method outlined in Section 3, we find a significant enhancement at $L \sim 10^8\, h^{-2}\, L_{\odot}$ in the low-redshift bin compared with that of the Y1-BGS subsample. To find the cause of the big enhancement, we checked the redshift distribution of galaxies in the 20 rosettes of the SV3-BGS

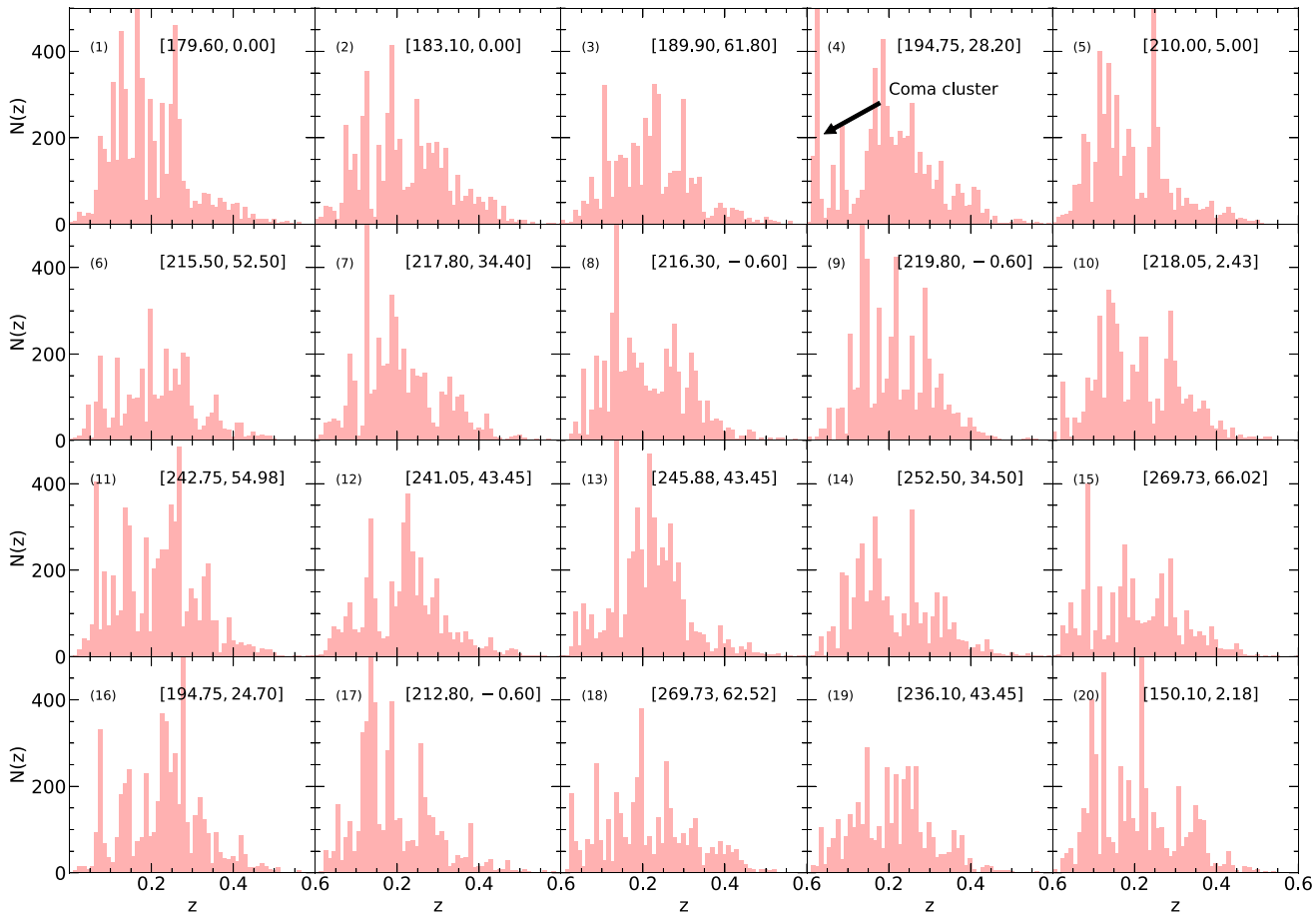

Figure A1. Redshift distribution of galaxies in 20 rosettes from SV3 (1% sky coverage) within the r-band magnitude 19.5 cut. The fourth rosette at the coordinate position [194.75, 28.20] contains the Coma cluster.

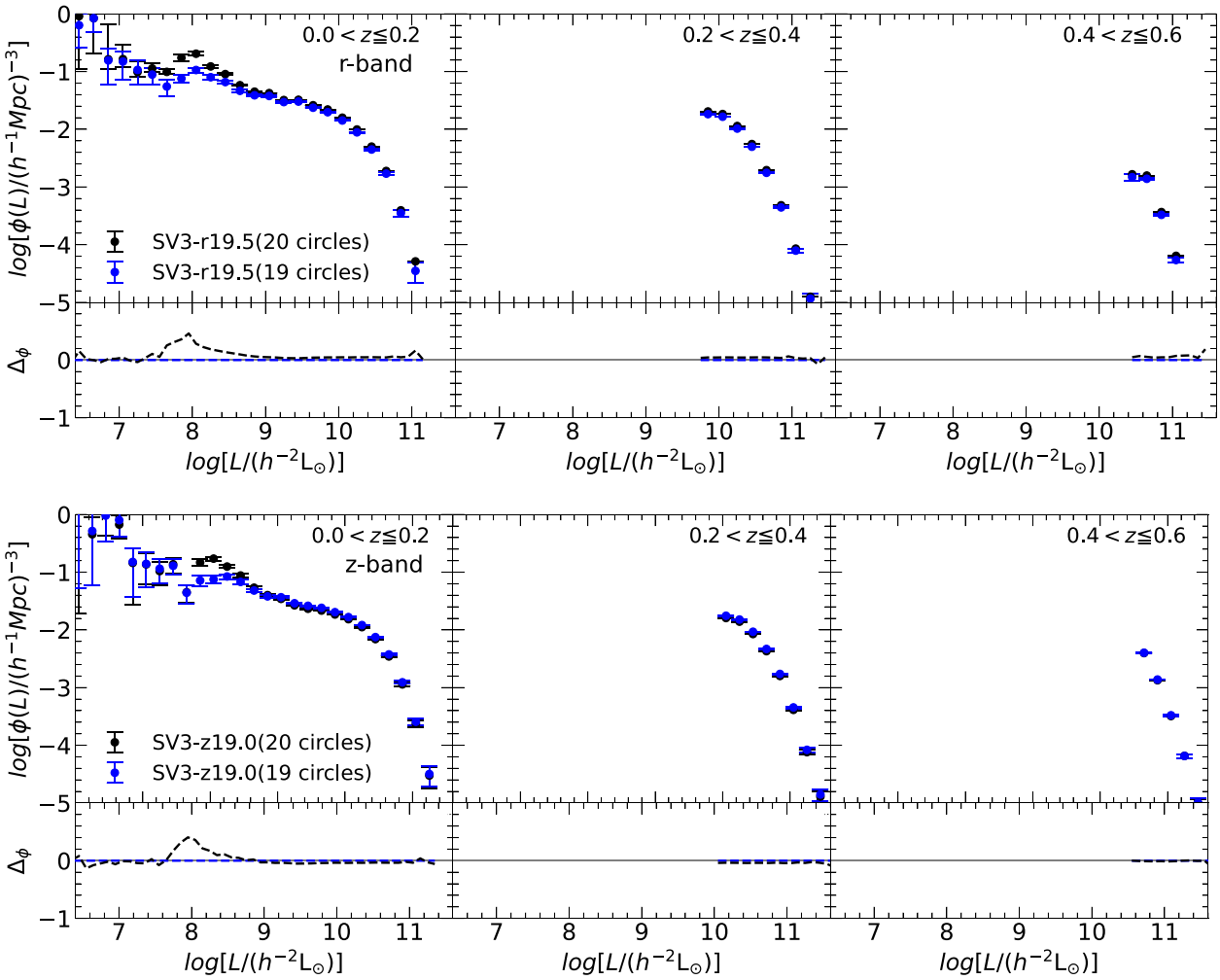

Figure A2. Comparison of LFs obtained from 20 and 19 (excluding the fourth) rosettes in the SV3-BGS subsamples.

subsample. The results are shown in different panels of Figure A1, each corresponding to a particular rosette. In several panels, spikes exhibit at low redshift, especially in panel (4), which is centered at the coordinate [R.A. = 194.75, decl. = 28.20]. According to the DESI official website,[42] this fourth rosette contains the Coma cluster with redshift ∼0.0231.

The presence of the Coma cluster significantly enhanced the LF measurements of the SV3-BGS subsample at $L \sim 10^8\, h^{-2}\, L_{\odot}$, which is verified in Figure A2. The black dots with error bars stand for the results with 20 rosettes, and the blue ones are the measurements with 19 rosettes excluding the Coma cluster one. Since the number of large clusters in the local Universe below the redshift of 0.03 is small, the Coma cluster causes a considerable cosmic variance in the DESI SV3-BGS 1% sky coverage. Thus, in our investigation, the galaxies in rosette 4 are excluded from our SV3-BGS subsample.

Appendix B
Spectroscopic and Photometric Redshift Distribution of SV3-BGS Galaxies

As illustrated in Section 4.1, the Gaussian distribution of photo-z fails to mimic the diminishing trend of LFs at the faint end within the lowest redshift bin. Consequently, we investigate the actual photo-z distribution for galaxies in the SV3-BGS sample. Displayed in each panel of Figure B1 are the observed spectroscopic and photometric redshift distributions for SV3-BGS galaxies with an apparent magnitude of $18.5 < r < 19.5$. The photo-zs for all galaxies were provided by Zhou et al. (2021). In comparison to the spectroscopic redshifts, the photo-z distribution at the lowest spectroscopic redshift peak in each panel tends to shift toward higher redshifts.

[42] https://desi.lbl.gov/trac/wiki/SurveyOps/OnePercent

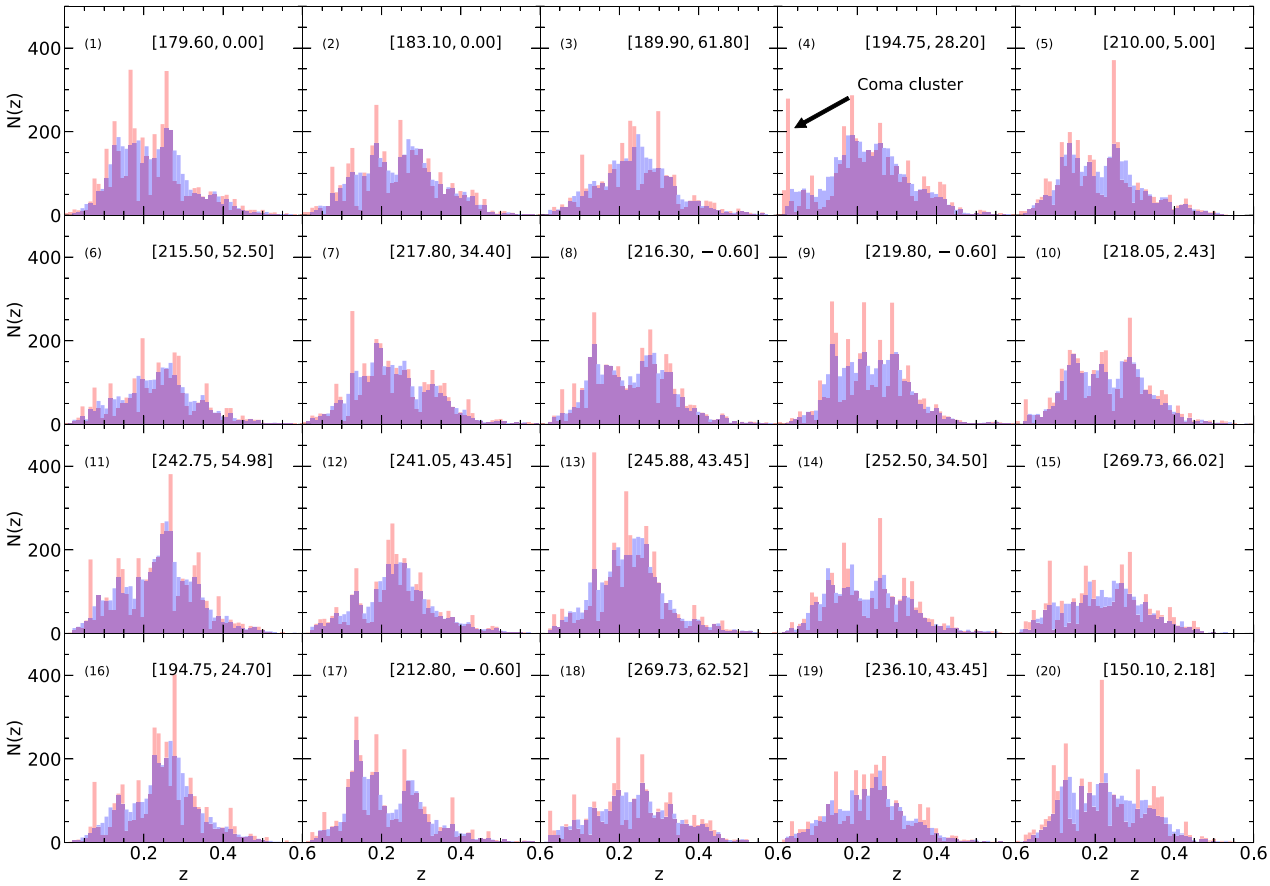

Figure B1. Redshift distribution of galaxies in 20 rosettes from SV3 (1% sky coverage) within the *r*-band magnitude 18.5 ∼19.5 cut. Red and blue histograms show the spec-*z* and photo-*z* distributions, respectively.

ORCID iDs

Yirong Wang (王艺蓉) https://orcid.org/0000-0003-3203-3299
Xiaohu Yang (杨小虎) https://orcid.org/0000-0003-3997-4606
Yizhou Gu (顾一舟) https://orcid.org/0000-0003-3196-7938
Haojie Xu (许浩杰) https://orcid.org/0000-0003-1132-8258
Yuyu Wang (王钰钰) https://orcid.org/0000-0002-0245-8547
Jiaxin Han (韩家信) https://orcid.org/0000-0002-8010-6715
Min He (何敏) https://orcid.org/0000-0001-6139-7660
Yunliang Zheng (郑云亮) https://orcid.org/0000-0002-5632-9345
Hu Zou (邹虎) https://orcid.org/0000-0002-6684-3997
ChangHoon Hahn https://orcid.org/0000-0003-1197-0902
Steven Ahlen https://orcid.org/0000-0001-6098-7247
David Brooks https://orcid.org/0000-0002-8458-5047
Shaun Cole https://orcid.org/0000-0002-5954-7903
Axel de la Macorra https://orcid.org/0000-0002-1769-1640
Biprateep Dey https://orcid.org/0000-0002-5665-7912
Jaime E. Forero-Romero https://orcid.org/0000-0002-2890-3725
Theodore Kisner https://orcid.org/0000-0003-3510-7134
Marc Manera https://orcid.org/0000-0003-4962-8934
Aaron Meisner https://orcid.org/0000-0002-1125-7384
Ramon Miquel https://orcid.org/0000-0002-6610-4836
John Moustakas https://orcid.org/0000-0002-2733-4559
Jundan Nie https://orcid.org/0000-0001-6590-8122
Claire Poppett https://orcid.org/0000-0003-0512-5489
Mehdi Rezaie https://orcid.org/0000-0001-5589-7116
Eusebio Sanchez https://orcid.org/0000-0002-9646-8198
Gregory Tarlé https://orcid.org/0000-0003-1704-0781
Zhimin Zhou https://orcid.org/0000-0002-4135-0977

References

Alam, S., Peacock, J. A., Kraljic, K., Ross, A. J., & Comparat, J. 2020, MNRAS, 497, 581
Alexander, D. M., Davis, T. M., Chaussidon, E., et al. 2023, AJ, 165, 124
Allende Prieto, C., Cooper, A. P., Dey, A., et al. 2020, RNAAS, 4, 188
Astropy Collaboration, Price-Whelan, A. M., Sipőcz, B. M., et al. 2018, AJ, 156, 123
Baldry, I. K., Driver, S. P., Loveday, J., et al. 2012, MNRAS, 421, 621
Behroozi, P. S., Conroy, C., & Wechsler, R. H. 2010, ApJ, 717, 379
Behroozi, P. S., Wechsler, R. H., & Conroy, C. 2013, ApJ, 770, 57
Blanton, M. R., Hogg, D. W., Bahcall, N. A., et al. 2003, ApJ, 592, 819
Blanton, M. R., Lupton, R. H., Schlegel, D. J., et al. 2005, ApJ, 631, 208
Blanton, M. R., & Roweis, S. 2007, AJ, 133, 734
Boquien, M. 2020, AAS Meeting, 235, 228.01
Brodzeller, A., Dawson, K., Bailey, S., et al. 2023, AJ, 166, 66
Brown, M. J. I., Zheng, Z., White, M., et al. 2008, ApJ, 682, 937
Bruzual, G., & Charlot, S. 2003, MNRAS, 344, 1000
Cacciato, M., van den Bosch, F. C., More, S., et al. 2009, MNRAS, 394, 929
Chaussidon, E., Yèche, C., Palanque-Delabrouille, N., et al. 2023, ApJ, 944, 107
Chen, Y., Mo, H. J., Li, C., et al. 2019, ApJ, 872, 180
Colless, M. 1999, RSPTA, 357, 105
Conroy, C. 2013, ARA&A, 51, 393
Conroy, C., Gunn, J. E., & White, M. 2009, ApJ, 699, 486
Conroy, C., Wechsler, R. H., & Kravtsov, A. V. 2006, ApJ, 647, 201
Cooper, A. P., Koposov, S. E., Allende Prieto, C., et al. 2023, ApJ, 947, 37
Davis, M., Efstathiou, G., Frenk, C. S., & White, S. D. M. 1985, ApJ, 292, 371
DESI Collaboration, Abareshi, B., Aguilar, J., et al. 2022, AJ, 164, 207
DESI Collaboration, Adame, A. G., Aguilar, J., et al. 2023, arXiv:2306.06307

DESI Collaboration, Adame, A. G., Aguilar, J., et al. 2024, AJ, 167, 62
DESI Collaboration, Aghamousa, A., Aguilar, J., et al. 2016a, arXiv:1611.00036
DESI Collaboration, Aghamousa, A., Aguilar, J., et al. 2016b, arXiv:1611.00037
Dey, A., Schlegel, D. J., Lang, D., et al. 2019, AJ, 157, 168
Dragomir, R., Rodríguez-Puebla, A., Primack, J. R., & Lee, C. T. 2018, MNRAS, 476, 741
Gao, H., Jing, Y. P., Gui, S., et al. 2023, ApJ, 954, 207
Golden-Marx, J. B., Zu, Y., Wang, J., et al. 2023, MNRAS, 524, 4455
Górski, K. M., Hivon, E., Banday, A. J., et al. 2005, ApJ, 622, 759
Gu, Y., Yang, X., Han, J., et al. 2024, MNRAS, 529, 4015
Guo, H., Zheng, Z., Behroozi, P. S., et al. 2016, MNRAS, 459, 3040
Guy, J., Bailey, S., Kremin, A., et al. 2023, AJ, 165, 144
Hahn, C.-H., Wilson, M. J., Ruiz-Macias, O., et al. 2023, AJ, 165, 253
Hahn, C., Aguilar, J. N., Alam, S., et al. 2024, ApJ, 963, 56
Han, J., Cole, S., Frenk, C. S., Benitez-Llambay, A., & Helly, J. 2018, MNRAS, 474, 604
Han, J., Jing, Y. P., Wang, H., & Wang, W. 2012, MNRAS, 427, 2437
Huchra, J. P., Macri, L. M., Masters, K. L., et al. 2012, ApJS, 199, 26
Hunter, J. D. 2007, CSE, 9, 90
Jing, Y. P., Mo, H. J., & Börner, G. 1998, ApJ, 494, 1
Katsianis, A., Xu, H., Yang, X., et al. 2021, MNRAS, 500, 2036
Katsianis, A., Yang, X., Fong, M., & Wang, J. 2023, MNRAS, 523, 1538
Kauffmann, G., Heckman, T. M., White, S. D. M., et al. 2003, MNRAS, 341, 33
Kewley, L. J., Dopita, M. A., Sutherland, R. S., Heisler, C. A., & Trevena, J. 2001, ApJ, 556, 121
Lan, T.-W., Ménard, B., & Mo, H. 2016, MNRAS, 459, 3998
Lan, T.-W., Tojeiro, R., Armengaud, E., et al. 2023, ApJ, 943, 68
Lang, D., Hogg, D. W., & Mykytyn, D. 2016, The Tractor: Probabilistic astronomical source detection and measurement, Astrophysics Source Code Library, ascl:1604.008
Lehmann, B. V., Mao, Y.-Y., Becker, M. R., Skillman, S. W., & Wechsler, R. H. 2017, ApJ, 834, 37
Levi, M., Bebek, C., Beers, T., et al. 2013, arXiv:1308.0847
Li, C., & White, S. D. M. 2009, MNRAS, 398, 2177
Lim, S. H., Mo, H. J., Lu, Y., Wang, H., & Yang, X. 2017, MNRAS, 470, 2982
Loveday, J., Norberg, P., Baldry, I. K., et al. 2015, MNRAS, 451, 1540
Lu, Y., Yang, X., & Shen, S. 2015, ApJ, 804, 55
Meng, J., Li, C., Mo, H. J., et al. 2023, ApJ, 944, 75
Miller, T. N., Doel, P., Gutierrez, G., et al. 2023, arXiv:2306.06310
Moster, B. P., Naab, T., & White, S. D. M. 2018, MNRAS, 477, 1822
Moustakas, J. 2023, FastSpecFit: Fast spectral synthesis and emission-line fitting of DESI spectra, Astrophysics Source Code Library, ascl:2308.005
Moustakas, J., Coil, A. L., Aird, J., et al. 2013, ApJ, 767, 50
Moustakas, J., Lang, D., Dey, A., et al. 2023, ApJS, 269, 3
Myers, A. D., Moustakas, J., Bailey, S., et al. 2023, AJ, 165, 50
Naab, T., & Ostriker, J. P. 2017, ARA&A, 55, 59
Neistein, E., Li, C., Khochfar, S., et al. 2011, MNRAS, 416, 1486
Norberg, P., Baugh, C. M., Hawkins, E., et al. 2002, MNRAS, 332, 827
Old, L., Skibba, R. A., Pearce, F. R., et al. 2014, MNRAS, 441, 1513
Old, L., Wojtak, R., Mamon, G. A., et al. 2015, MNRAS, 449, 1897
Peacock, J. A., & Smith, R. E. 2000, MNRAS, 318, 1144
Perez, F., & Granger, B. E. 2007, CSE, 9, 21
Planck Collaboration, Aghanim, N., Akrami, Y., et al. 2020, A&A, 641, A6
Raichoor, A., Eisenstein, D. J., Karim, T., et al. 2020, RNAAS, 4, 180
Raichoor, A., Moustakas, J., Newman, J. A., et al. 2023, AJ, 165, 126
Reddick, R. M., Wechsler, R. H., Tinker, J. L., & Behroozi, P. S. 2013, ApJ, 771, 30
Rodríguez-Puebla, A., Avila-Reese, V., & Drory, N. 2013, ApJ, 767, 92
Rodríguez-Puebla, A., Avila-Reese, V., Yang, X., et al. 2015, ApJ, 799, 130
Rodríguez-Puebla, A., Calette, A. R., Avila-Reese, V., Rodriguez-Gomez, V., & Huertas-Company, M. 2020, PASA, 37, e024
Ruiz-Macias, O., Zarrouk, P., Cole, S., et al. 2020, RNAAS, 4, 187
Sales, L. V., Wetzel, A., & Fattahi, A. 2022, NatAs, 6, 897
Schlafly, E. F., Kirkby, D., Schlegel, D. J., et al. 2023, AJ, 166, 259
Silber, J. H., Fagrelius, P., Fanning, K., et al. 2023, AJ, 165, 9
Skibba, R. A., van den Bosch, F. C., Yang, X., et al. 2011, MNRAS, 410, 417
Smercina, A., Bell, E. F., Price, P. A., et al. 2018, ApJ, 863, 152
Song, J., Fang, G., Lin, Z., Gu, Y., & Kong, X. 2023, ApJ, 958, 82
Springel, V. 2005, MNRAS, 364, 1105
Springel, V., Yoshida, N., & White, S. D. M. 2001, NewA, 6, 79
Taylor, M. B. 2005, in ASP Conf. Ser. 347, Astronomical Data Analysis Software and Systems XIV, ed. P. Shopbell et al. (San Francisco, CA: ASP), 29
The Dark Energy Survey Collaboration 2005, arXiv:astro-ph/0510346
Tinker, J. L. 2021, ApJ, 923, 154
Tinker, J. L., Cao, J., Alpaslan, M., et al. 2021, MNRAS, 505, 5370
Tinker, J. L., Weinberg, D. H., Zheng, Z., & Zehavi, I. 2005, ApJ, 631, 41
To, C.-H., Reddick, R. M., Rozo, E., Rykoff, E., & Wechsler, R. H. 2020, ApJ, 897, 15
Vale, A., & Ostriker, J. P. 2004, MNRAS, 353, 189
van den Bosch, F. C., Yang, X., & Mo, H. J. 2003, MNRAS, 340, 771
van den Bosch, F. C., Yang, X., Mo, H. J., et al. 2007, MNRAS, 376, 841
Wang, H., Mo, H. J., Yang, X., et al. 2016, ApJ, 831, 164
Wang, L., Yang, X., Shen, S., et al. 2014, MNRAS, 439, 611
Wang, W., Takada, M., Li, X., et al. 2021, MNRAS, 500, 3776
Wang, Y., Yang, X., Mo, H. J., & van den Bosch, F. C. 2007, ApJ, 664, 608
Wang, Z., Xu, H., Yang, X., et al. 2019, ApJ, 879, 71
Wechsler, R. H., & Tinker, J. L. 2018, ARA&A, 56, 435
Willmer, C. N. A. 2018, ApJS, 236, 47
Xu, H., Zheng, Z., Yang, X., & Li, Q. 2023, arXiv:2311.04966
Xu, K., Jing, Y. P., & Gao, H. 2022, ApJ, 939, 104
Yang, X., Mo, H. J., Jing, Y. P., & van den Bosch, F. C. 2005a, MNRAS, 358, 217
Yang, X., Mo, H. J., & van den Bosch, F. C. 2003, MNRAS, 339, 1057
Yang, X., Mo, H. J., & van den Bosch, F. C. 2008, ApJ, 676, 248
Yang, X., Mo, H. J., & van den Bosch, F. C. 2009, ApJ, 695, 900
Yang, X., Mo, H. J., van den Bosch, F. C., et al. 2007, ApJ, 671, 153
Yang, X., Mo, H. J., van den Bosch, F. C., & Jing, Y. P. 2005b, MNRAS, 356, 1293
Yang, X., Mo, H. J., van den Bosch, F. C., Zhang, Y., & Han, J. 2012, ApJ, 752, 41
Yang, X., Xu, H., He, M., et al. 2021, ApJ, 909, 143
Yang, X., Zhang, Y., Wang, H., et al. 2018, ApJ, 860, 30
Yèche, C., Palanque-Delabrouille, N., Claveau, C.-A., et al. 2020, RNAAS, 4, 179
York, D. G., Adelman, J., Anderson, J. E. J., et al. 2000, AJ, 120, 1579
Yuan, S., Eisenstein, D. J., & Garrison, L. H. 2018, MNRAS, 478, 2019
Yuan, S., Garrison, L. H., Hadzhiyska, B., Bose, S., & Eisenstein, D. J. 2022, MNRAS, 510, 3301
Zehavi, I., Zheng, Z., Weinberg, D. H., et al. 2005, ApJ, 630, 1
Zehavi, I., Zheng, Z., Weinberg, D. H., et al. 2011, ApJ, 736, 59
Zhan, H. 2011, SSPMA, 41, 1441
Zhan, H. 2018, 42nd COSPAR Scientific Assembly, E1.16–4–18
Zhao, P., Xu, H., Katsianis, A., & Yang, X.-H. 2020, RAA, 20, 195
Zheng, Z., Berlind, A. A., Weinberg, D. H., et al. 2005, ApJ, 633, 791
Zheng, Z., Zehavi, I., Eisenstein, D. J., Weinberg, D. H., & Jing, Y. P. 2009, ApJ, 707, 554
Zhou, R., Dey, B., Newman, J. A., et al. 2023, AJ, 165, 58
Zhou, R., Newman, J. A., Dawson, K. S., et al. 2020, RNAAS, 4, 181
Zhou, R., Newman, J. A., Mao, Y.-Y., et al. 2021, MNRAS, 501, 3309
Zou, H., Gao, J., Zhou, X., & Kong, X. 2019, ApJS, 242, 8
Zou, H., Zhou, X., Fan, X., et al. 2017, PASP, 129, 064101
Zu, Y., & Mandelbaum, R. 2015, MNRAS, 454, 1161
Zu, Y., & Mandelbaum, R. 2016, MNRAS, 457, 4360
Zu, Y., & Mandelbaum, R. 2018, MNRAS, 476, 1637